iScience

Article

In-depth functional analysis of BRD9 in fetal hematopoiesis reveals context-dependent roles

Graphical abstract

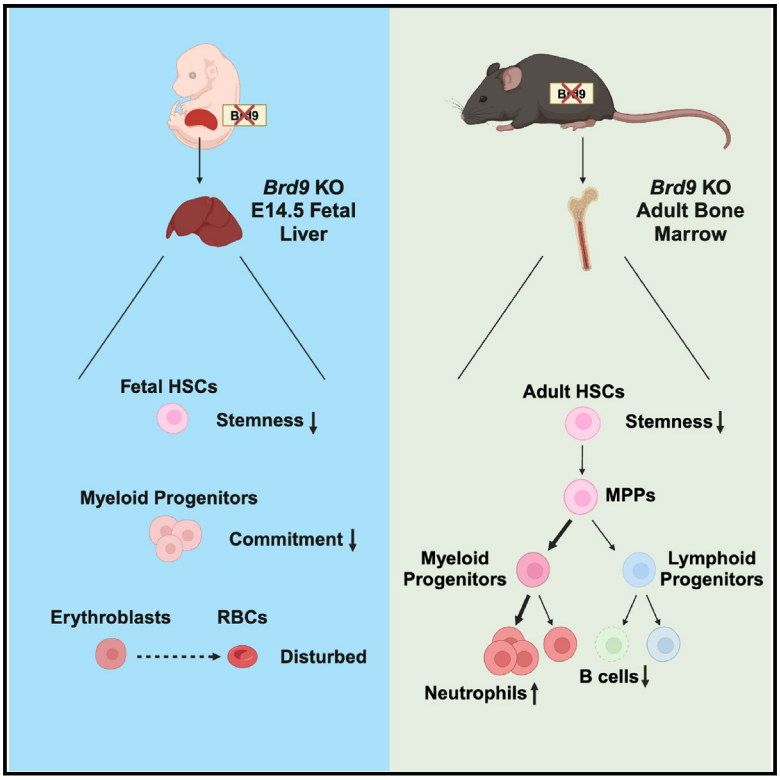

Highlights

- BRD9 depletion compromises both the quality and quantity of fetal HSCs
- The roles of BRD9 in differentiation are lineage- and stage-dependent
- Integrated analysis unveils distinct functions of BRD9 in hematopoiesis
- Single-cell transcriptome of HSCs elucidates BRD9's roles in lineage commitment

Authors

Yifan Zhang, Masaki Nomura, Koutarou Nishimura, ..., Hiromi Yamazaki, Akifumi Takaori-Kondo, Daichi Inoue

Correspondence

nishimura.koutarou.pww@osaka-u.ac.jp (K.N.),
d-inoue@patho.med.osaka-u.ac.jp (D.I.)

In brief

Cell biology; Molecular biology; Omics

Zhang et al., 2025, iScience *28*, 112010
March 21, 2025
https://doi.org/10.1016/j.isci.2025.112010

CellPress

iScience

CellPress
OPEN ACCESS

Article

In-depth functional analysis of BRD9 in fetal hematopoiesis reveals context-dependent roles

Yifan Zhang,[1,2,8] Masaki Nomura,[1,3,4,8] Koutarou Nishimura,[1,4,*] Weijia Zang,[1,2,4] Yui Koike,[1,4] Muran Xiao,[1] Hiromi Ito,[1,4] Miki Fukumoto,[1] Atsushi Tanaka,[1] Yumi Aoyama,[1,2] Wataru Saika,[1,4,5] Chihiro Hasegawa,[1,4,6] Hiromi Yamazaki,[1,4] Akifumi Takaori-Kondo,[2] and Daichi Inoue[1,2,4,7,9,*]

[1]Department of Hematology-Oncology, Institute of Biomedical Research and Innovation, Foundation for Biomedical Research and Innovation at Kobe, Kobe, Japan
[2]Department of Hematology, Graduate School of Medicine, Kyoto University, Kyoto, Japan
[3]Facility for iPS Cell Therapy, CiRA Foundation, Kyoto, Japan
[4]Department of Cancer Pathology, Graduate School of Medicine and Frontier Biosciences, Osaka University, Suita, Japan
[5]Department of Hematology, Shiga University of Medical Science, Otsu, Japan
[6]Department of Hematology and Oncology, Graduate School of Medicine, Osaka University, Suita, Japan
[7]Institute for Open and Transdisciplinary Research Initiatives, Osaka University, Suita, Japan
[8]These authors contributed equally
[9]Lead contact
*Correspondence: nishimura.koutarou.pww@osaka-u.ac.jp (K.N.), d-inoue@patho.med.osaka-u.ac.jp (D.I.)
https://doi.org/10.1016/j.isci.2025.112010

SUMMARY

The hierarchical organization of hematopoietic stem cells (HSCs) governing adult hematopoiesis has been extensively investigated. However, the dynamic epigenomic transition from fetal to adult hematopoiesis remains incompletely understood, particularly regarding the involvement of epigenetic factors. In this study, we investigate the roles of BRD9, an essential component of the non-canonical BAF (ncBAF) complex known to govern the fate of adult HSCs, in fetal hematopoiesis. Consistent with observations in adult hematopoiesis, BRD9 loss impairs fetal HSC stemness and disturbs erythroid maturation. Intriguingly, the impact on myeloid lineage was discrepant: BRD9 loss inhibited and promoted myeloid differentiation in fetal and adult models, respectively. Through comprehensive transcriptomic and epigenomic analysis, we elucidate the differential roles of BRD9 in a context- and lineage-dependent manner. Our data uncover how BRD9/ncBAF complex modulates transcription in a stage-specific manner, providing deeper insights into the epigenetic regulation underlying the transition from fetal to adult hematopoiesis.

INTRODUCTION

Hematopoiesis is a continuous process where hematopoietic stem cells (HSCs) are positioned at the top of the hierarchy, giving rise to lineage-committed progenitors, including myeloid progenitors (which develop into monocytes, neutrophils, basophils, eosinophils, erythrocytes, and megakaryocytes) and lymphoid progenitors (which differentiate into T cells, B cells, and natural killer cells).[1,2] This hierarchical model, established through cell surface marker analysis, colony formation assays, and transplantation assays, explains how blood cells mature in the adult bone marrow (BM)[3–5] and provides foundational insights for anemia and leukemia treatments. However, recent discoveries suggest that the hematopoietic process in the fetus differs from that in adults. The fetal hematopoietic process consists of multiple waves in mice[6]: (1) primitive hematopoiesis arises from the E7.5 yolk sac, generating short-lived erythrocytes and megakaryocytes. (2) The second, or pro-definitive, wave originates from the E8.25 yolk sac. Erythro-myeloid progenitors (EMPs) from this wave colonize the fetal liver (FL) and establish blood circulation until birth. (3) Definitive hematopoiesis begins in the E10.5 aorta-gonad-mesonephros (AGM) region, where the first HSCs are formed. These HSCs soon migrate to the fetal liver for expansion and maturation before permanently colonizing the BM to support adult hematopoiesis. A recent paradigm shift has emerged in understanding the formation and transition of this hematopoietic hierarchy,[7] presenting new biological propositions that require further investigation.

The mechanisms underlying the differences between adult and fetal hematopoiesis have attracted significant research interest. Recent studies have explored the three-dimensional (3D) genome organization of adult and fetal HSCs to uncover these mechanisms. Dynamic chromatin changes occur during the transition from fetal to adult stages.[8] However, the specific chromatin remodelers involved in this process still need to be clarified. SWI/SNF complexes, ATP-dependent chromatin remodelers, play critical roles in gene regulation by modulating chromatin architecture and DNA accessibility.[9–12] These complexes are categorized into three subcomplexes: canonical

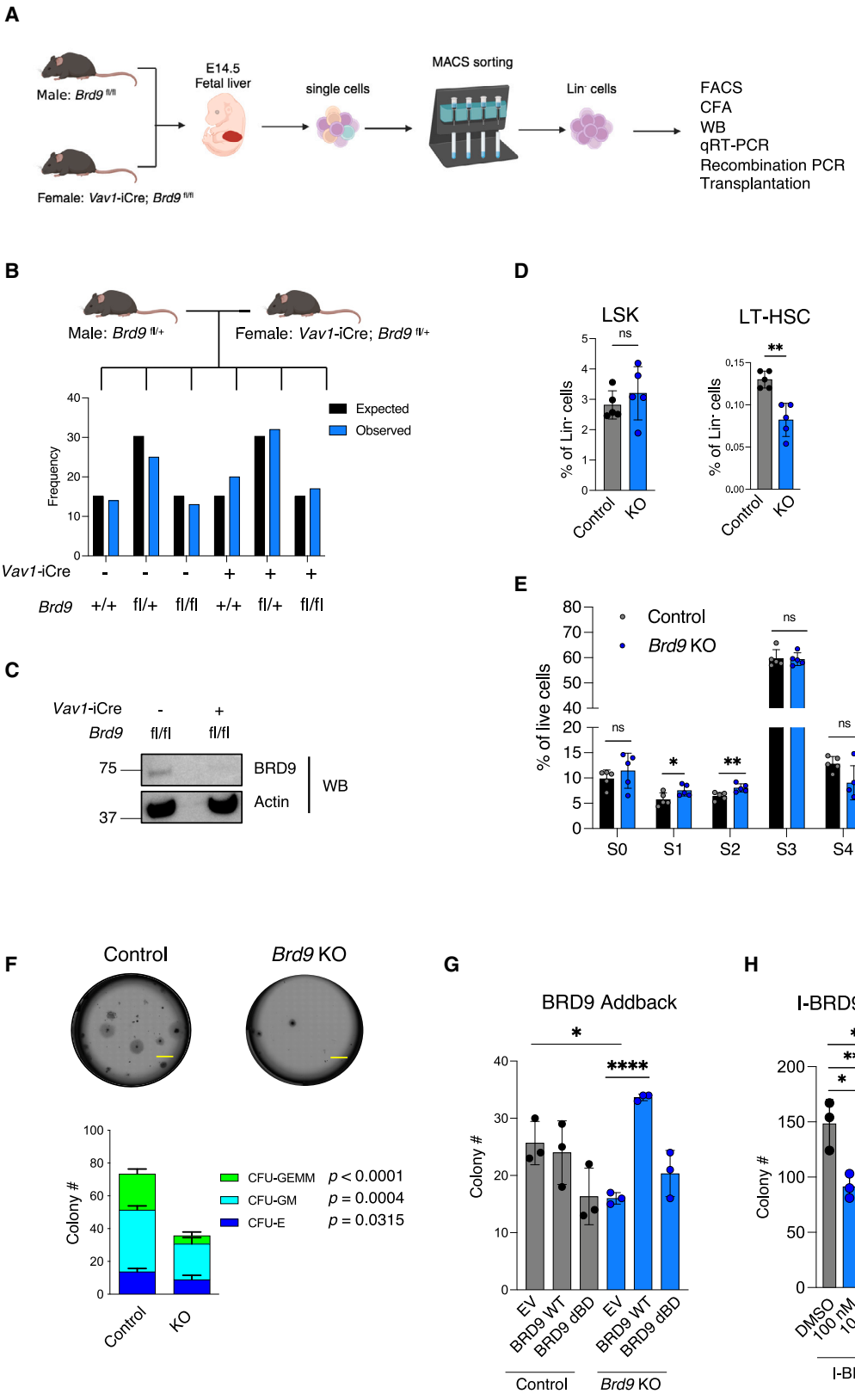

(legend on next page)

BAF (cBAF), polybromo BAF (PBAF), and the newly identified non-canonical BAF (ncBAF, also known as GBAF), each with unique functions.[13–17] Previous researches have demonstrated the crucial roles of BAF complex members in fetal hematopoiesis. For example, mice lacking the PBAF-specific member ARID2 exhibit impaired long-term hematopoietic reconstitution,[18] and the pan-BAF catalytic subunit BRG1 is essential for fetal erythroid maturation and hemoglobin production.[19] Additionally, the cBAF-specific ARID1A regulates the pool size of FL HSCs.[20] The *Smarca2* gene, which encodes the pan-BAF catalytic subunit BRM, is upregulated as fetal-to-adult switching due to increasing enhancer-promoter interactions.[8] Despite these findings related to the BAF complex, the precise genetic contributions of ncBAF components to fetal hematopoiesis and the fetal-to-adult transition remain unclear, necessitating detailed investigations.

Bromodomain containing 9 (BRD9) is a unique member of the ncBAF complex.[16,21] Besides its critical roles in mouse and human pluripotent stem cells, we have previously shown that BRD9 is essential for normal adult hematopoiesis[16,22] and that BRD9 is substantially downregulated due to mRNA degradation from mis-splicing by mutations in the spliceosomal protein, SF3B1.[23,24] Post-natal BRD9 loss impairs HSC stemness, significantly inhibits B cell development and promotes myeloid differentiation. BRD9-deficient mice exhibit a myelodysplastic syndrome (MDS) phenotype with aged HSCs. These are linked to BRD9's role in chromatin regulation, particularly in myeloid-related genome locus, further underscoring the ncBAF complexes' function in 3D chromatin regulation and normal stem cell biology.[17] In this study, we explored the role of BRD9 in fetal hematopoiesis. While BRD9 knockout (KO) in fetal hematopoietic cells similarly impairs the stemness of HSCs, it uniquely inhibits myeloid differentiation, contrary to observations in adult hematopoiesis. Comprehensive transcriptomic and chromatin analysis highlighted the differential roles of BRD9 in lineage commitment during fetal versus adult hematopoiesis, providing deeper insights into the time- and context-dependent functions of ncBAF in blood production.

RESULTS

Generation and characterization of *Vav1*-iCre; *Brd9*$^{fl/fl}$ mouse model

To investigate how BRD9 contributes to fetal hematopoiesis, we generated the *Vav1*-iCre; *Brd9*$^{fl/fl}$ mouse, which allows blood-specific and conditional KO of *Brd9* in hematopoietic compartments from embryonic day 9.5 (E9.5)[25–27] (Figure 1A). Following the mating of *Brd9*$^{fl/+}$ males with *Vav1*-iCre; *Brd9*$^{fl/+}$ females, *Vav1*-iCre; *Brd9*$^{fl/fl}$ mice were born at the expected Mendelian ratio, indicating that *Brd9* deletion in hematopoietic cells is not essential for fetal development (Figures 1B and S1A). To further investigate the function of BRD9 in embryos, we harvested fetal liver (FL) from E14.5 fetuses because this time point is considered to be when hematopoiesis is at its peak in the liver.[28] In this newly generated KO model, we confirmed almost undetectable levels of *Brd9* mRNA and protein in E14.5 FL lineage-negative cells (Lin$^-$ cells: CD3ε$^-$, CD4$^-$, CD8a$^-$, CD19$^-$, NK1.1$^-$, Gr-1$^-$, and Ter-119$^-$) and the expected recombination of floxed allele (Figures 1C, S1B, and S1C). There were no significant alterations in fetus and FL weight or in FL cellularity in the KO group (Figure S1D). Similarly, no apparent defects were observed in E14.5 fetuses or P7 pups (Figures S1E and S1F).

We next sought to evaluate how *Brd9* deletion affects the compartment of fetal hematopoietic stem and progenitor cells (HSPCs). FACS analysis was performed using cell surface markers to define the following hematopoietic progenitors fractions[29–31]: megakaryocyte-erythroid progenitors (MEP, CD34$^-$FcγR$^-$LK[Lin$^-$c-Kit$^+$]), common myeloid progenitors (CMP, CD34$^+$FcγR$^-$ LK), granulocyte-monocyte progenitors (GMP, CD34$^+$FcγR$^+$ LK) and common lymphoid progenitors (CLP, Lin$^-$Sca-1^{int}c-Kit^{int}CD127$^+$CD135$^+$); MPP/HSC fractions: MPP2 (CD135$^-$CD150$^+$CD48$^+$ LSK [Lin$^-$Sca-1$^+$c-Kit$^+$]), MPP3 (CD135$^-$CD150$^-$CD48$^+$ LSK), MPP4 (CD135$^+$CD150$^-$ LSK), ST-HSC (CD135$^-$CD150$^-$CD48$^-$ LSK), and LT-HSC (CD135$^-$CD150$^+$CD48$^-$ LSK). We observed a significant reduction in LT-HSCs and a simultaneous increase in ST-HSCs in the KO group, although there was no significant change in the overall frequency of LSK cells (Figure 1D). Among other progenitors,

Figure 1. Generation and characterization of *Vav1*-iCre; *Brd9*$^{fl/fl}$ mouse model

(A) Schematic representation of *Vav1*-iCre; *Brd9*$^{fl/fl}$ fetal liver (FL) experiments. Day 0.5 of pregnancy (E0.5) was defined as the morning on the day of a vaginal plug confirmation. Lin$^-$ cells were isolated from E14.5 FL by MACS selection.

(B) Offspring genotype frequency. Mating pairs were *Brd9*$^{fl/+}$ male mice and *Vav1*-iCre; *Brd9*$^{fl/+}$ female mice (Offspring $n = 121$).

(C) Western blot analysis for murine BRD9 and ACTB in E14.5 FL Lin$^-$ cells derived from *Brd9*$^{fl/fl}$ (Control) fetus and *Vav1*-iCre; *Brd9*$^{fl/fl}$ (*Brd9* KO) fetuses (Representative images of three independent experiments).

(D) Flow cytometric analysis of E14.5 FL cells to evaluate the frequency of stem and progenitor fraction, including LSKs (Lin$^-$c-Kit$^+$Sca-1$^+$ cells), LT-HSCs (CD150$^+$CD48$^-$CD135$^-$ LSKs), and ST-HSCs (CD150$^-$CD48$^-$CD135$^-$ LSKs). $n = 5$ fetuses for each group, independent samples; data are represented as mean ± s.e.m. $^*p < 0.05$, $^{**}p < 0.01$; ns, not significant ($p > 0.05$); the p values were calculated by two-tailed unpaired t test.

(E) Frequency of erythroid progenitors (S0-S5) in Control and *Brd9* KO FL cells. $n = 5$ fetuses for each group, independent experiments, data are represented as mean ± s.e.m. $^*p < 0.05$, $^{**}p < 0.01$; ns, not significant ($p > 0.05$); the p values were calculated by two-tailed unpaired t test.

(F) Colony formation assay (CFA) of E14.5 FL Lin$^-$ cells. Colonies were scored 10 days after plating in methylcellulose in M3434 for myeloid colonies. CFU-GEMM, CFU-GM, CFU-E were counted separately. Scale bar: 5mm. Control $n = 3$, *Brd9* KO $n = 6$ independent experiments; data are represented as mean ± s.e.m. The p values were calculated by two-tailed unpaired t test.

(G) Myeloid colony output from E14.5 FL Lin$^-$ cells transduced with BRD9 wild-type (WT) and bromodomain-deleted mutant (dBD) cDNA. Colonies were scored 10 days after plating in methylcellulose (MethoCult M3434) to assess myeloid colony formation. $n = 3$ independent experiments for each group; data are represented as mean ± s.e.m. $^*p < 0.05$, $^{****}p < 0.0001$; the p values were calculated by two-tailed unpaired t test.

(H) Myeloid colony output of wild-type E14.5 FL Lin$^-$ cells treated with DMSO or the indicated concentrations of I-BRD9. Colonies were scored 10 days after plating in methylcellulose (MethoCult M3434). $n = 3$ independent experiments for each group; data are represented as mean ± s.e.m. $^*p < 0.05$, $^{**}p < 0.01$, $^{***}p < 0.001$; the p values were calculated by two-tailed unpaired t test.

although MPPs were comparable between the groups, we found significantly reduced frequencies of MEP and a trend toward decreased numbers of myeloid and erythroid progenitors, including CMP, GMP, and MEP (Figures S2A and S2B). Additionally, in line with our previous findings showing a significant decrease in erythroid commitment signatures in adult KO HSPCs,[22] BRD9 loss disturbed erythroid maturation in KO FL samples. This was reflected by an increase in early erythroid stages (S1 and S2) and a decrease in more mature stages (S4 and S5), as estimated by CD71/Ter-119 positivity[32] (Figure 1E). In the myeloid mature fractions, we noted a comparable number of $CD11b^+$ cells in the *Brd9* KO samples (Figure S2C).

Our previous study demonstrated the pivotal roles of BRD9 in adult hematopoiesis. Specifically, BRD9 loss in adult hematopoiesis results in two distinct effects: a reduction in phenotypic LT-HSCs and altered lineage development, characterized by impaired B cell maturation with decreased pre-B cells and later stages, as well as enhanced neutrophil production, resulting in myeloid skewing.[22] To evaluate whether BRD9 loss in fetal hematopoiesis affects colony output, Lin^- cells from E14.5 FL were seeded in methylcellulose with cytokine cocktails (IL-3, IL-6, SCF, and EPO) that promote myeloid differentiation. Interestingly, we observed a significant decrease in various types of myeloid colonies (CFU-GEMM, CFU-GM, and CFU-E) in the KO group (Figure 1F). To assess colony output from specific progenitor populations, we plated FACS-sorted MEP, CMP, and GMP cells, revealing a significant reduction in colony formation (Figure S2D). Next, to further validate the role of BRD9 in myeloid colony development, we re-expressed full length of BRD9 (wild-type, WT) as well as bromodomain-deleted BRD9 mutant (dBD) in both Control and *Brd9* KO E14.5 FL Lin^- cells.[23] Interestingly, BRD9 WT, not dBD, rescued the impaired colony output caused by *Brd9* KO, indicating that BRD9's function is essential in a bromodomain-dependent manner (Figure 1G). Next, we assessed the effects of pharmacologically inhibiting the BRD9 bromodomain using I-BRD9, a potent and selective BRD9 inhibitor. We observed a dose-dependent reduction in myeloid colony formation from wild-type E14.5 FL Lin^- cells treated with I-BRD9 (Figure 1H).

Since BRD9 is a component of the ncBAF complex, we investigated whether these effects were due to the functional impairment of ncBAF. To address this, we transduced E14.5 FL Lin^- cells with shRNAs targeting *Brd9* or *Gltscr1* and observed a significant reduction in colony formation in both the sh*Brd9* and sh*Gltscr1* groups (Figures S2E and S2F), suggesting a direct involvement of the ncBAF complex in the observed phenotype. These results indicate that while *Brd9* KO in fetal hematopoietic cells does not affect fetal development, its deficiency significantly impairs the hematopoietic process, particularly in the myeloid and erythroid lineages.

Brd9 deletion profoundly impairs the stemness of FL HSCs

Considering the notable alteration in the HSC fraction, we next examined whether *Brd9* deficiency impairs the long-term reconstitution ability using a limiting dilution assay (LDA). E14.5 Lin^- FL cells derived from control ($Brd9^{fl/fl}$) or *Brd9* KO (*Vav1*-iCre; $Brd9^{fl/fl}$) were transplanted via tail injection into lethally irradiated B6.SJL ($CD45.1^+$) recipients under three conditions: 400K cells/recipient, 200K cells/recipient, and 50K cells/recipient (Figures 2A and 2B). With the dilution of transplanted Lin^- FL cells, the number of surviving recipients significantly decreased in the KO group (Figure 2B). These results indicate the impaired capacity of *Brd9* KO E14.5 FL cells to reconstitute in an adult BM environment. The estimated stem cell frequency[33,34] in the *Brd9* KO group is approximately one-tenth that of the control group, with frequencies of 1 in 824,419 cells and 1 in 87,867 cells, respectively (Figure 2C). This finding is further supported by the additional transplantation using LSK and LK cells. Lethally irradiated recipients transplanted with KO LK cells died significantly earlier (Figure S3A). When 3K LSK cells, which are more enriched for HSCs, were transplanted, nearly half of the KO group did not survive beyond two weeks, in contrast to the prolonged survival observed in the control group (Figure S3A). Intriguingly, in the survived recipients transplanted with FL Lin^- cell, we observed reduced frequencies and numbers of $CD45.2^+$ donor-derived LT-HSCs and ST-HSCs in the KO group, accompanied by a concomitant increase in the MPP3 fraction (Figures 2D and S3B–S3D), and a dramatic decrease in B cells ($B220^+$) and an increase in myeloid lineages ($CD11b^+Gr\text{-}1^+$ neutrophils and $CD11b^+Gr\text{-}1^-$ monocytes) in the peripheral blood (PB) and the spleen (Figures S4A and S4B). Additionally, genomic recombination and the undetectable levels of *Brd9* mRNA were confirmed in recipients transplanted with KO FL cells (Figures S4C and S4D), further reinforcing the differential behavior influenced by the hematopoietic microenvironment. The observed phenotypes of the engrafted FL HSC in the adult BM were consistent with our recent findings using adult *Mx1*-Cre; $Brd9^{fl/fl}$ mice, which allow for conditional, time-controlled, and efficient deletion of *Brd9* in postnatal hematopoietic cells.[23] Collectively, these results suggest that *Brd9* deficiency significantly impairs the reconstitution ability of E14.5 FL HSPCs. Despite losing their stemness, the engrafted KO FL cells exhibit a strong preference for myeloid lineage differentiation in adult BM circumstances.

Brd9 KO altered chromatin state and transcription, leading to disturbed HSC and myeloid program

Given the broad, multi-lineage disturbances associated with BRD9 loss in the hematopoietic system, we hypothesized that these defects originate from HSPCs. We, therefore, sought to evaluate the altered transcriptional program in HSPCs. RNA-seq analysis was performed on FACS-purified FL Lin^- cells of E14.5 control ($Brd9^{fl/fl}$) and KO (*Vav1*-iCre; $Brd9^{fl/fl}$) fetus. Contrary to our previous findings in the adult HSPCs,[22] the transcriptomic analysis revealed a larger number of genes downregulated in the KO group compared to those upregulated (370 genes vs. 12 genes, applying adjusted $p < 0.05$ and $|\log_2 FC| > 1$), resulting in distinct principal components (Figures 3A and S5A). Gene ontology (GO) analysis and gene set enrichment analysis (GSEA) indicated negative enrichment for pathways related to stemness of fetal HSCs and myeloid development (Figures 3B and S5B), consistent with the observed phenotypes such as impaired stemness and myeloid development in *Brd9* KO FL cells. Notably, critical genes related to HSCs[35] (*Kit*, *Slamf1*, *Cd48*, and *Vav3*) and myeloid lineage (*Camp*,[36] *Mpo*,[37]

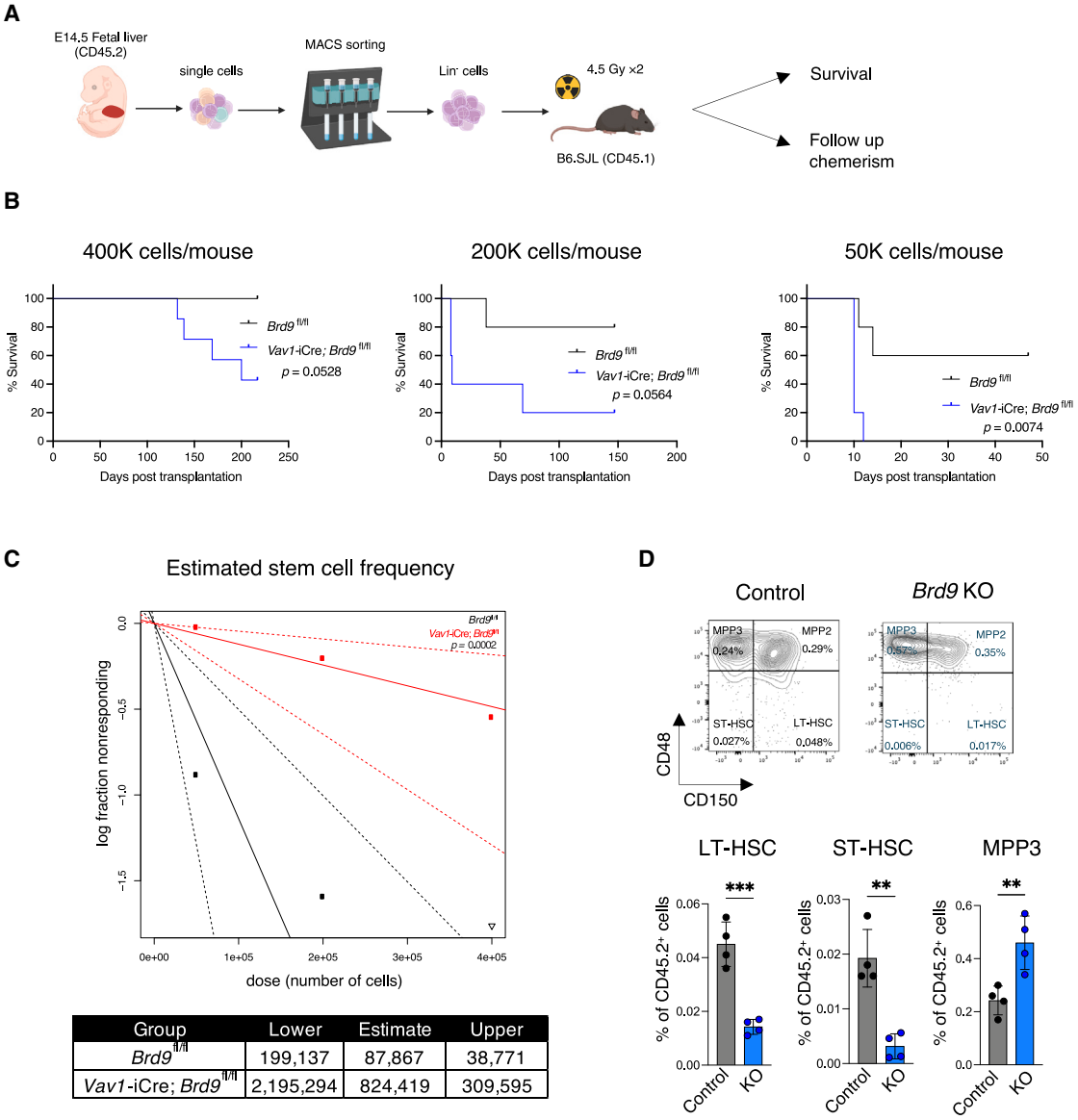

Group	Lower	Estimate	Upper
Brd9$^{fl/fl}$	199,137	87,867	38,771
Vav1-iCre; *Brd9*$^{fl/fl}$	2,195,294	824,419	309,595

Figure 2. *Brd9* deletion profoundly impairs the stemness of FL HSCs

(A) Schema for the transplant experiment. FL cells were derived from E14.5 control and *Brd9* KO fetus (CD45.2$^+$). Isolated single cells were proceeded to MACS selection to harvest Lin$^-$ cells. B6.SJL (CD45.1$^+$) recipient mice were injected with FL Lin$^-$ cells after lethal irradiation (4.5Gy × 2).

(B) Kaplan-Meier survival analysis of Limiting dilution assay (LDA). Recipient mice transplanted with control or *Brd9* KO FL Lin$^-$ cells of different cell numbers (400K cells/mouse, 200K cells/mouse, 50K cells/mouse). Recipient $n = 5$ mice for each group. The p values were calculated by log rank test.

(C) Estimated stem cell frequency calculated by LDA plot. The amount of initially transplanted cells (x axis) is plotted against the log fraction of non-responders corresponding to recipients not able to survival (y axis). The slope of the line represents the log-active cell fraction. The dash lines and the table display confidence intervals for estimated stem cell frequency. Recipient $n = 5$ mice for each group. The p values were calculated via ELDA.

(D) Representative FACS plots and frequency of BM cells from recipients transplanted with Control or *Brd9* KO E14.5 FL cells, MPP3s (CD150$^-$CD48$^+$CD135$^-$ LSK), MPP2 (CD150$^+$CD48$^+$CD135$^-$ LSK), LT-HSCs and ST-HSCs in CD45.2$^+$ population. Control $n = 4$ mice, *Brd9* KO $n = 4$ mice, independent experiments, data are represented as mean ± s.e.m. $^{**}p < 0.01$, $^{***}p < 0.001$ the p values were calculated by two-tailed unpaired t test.

Prss57,[38] *Elane*,[39] and *Spi*[40]) were downregulated in the *Brd9* KO group (Figures 3C and S5C), while erythroid-related genes and lymphoid-related genes showed no consistent alteration. The downregulated genes in the KO group were enriched in pathways related to neutrophil degranulation, innate immune system, and Toll-like receptor signaling pathway regulation (Figure S5D). Transcription factors (TFs) associated with downregulated genes included CEBPA, SPI, and MYB, which were consistent with the GSEA results (Figures 3B and S5D). Given that a large portion of differently expressed genes (DEGs) were downregulated in the KO group and that BRD9 is regarded as an essential component of the ncBAF complex, one of the mammalian

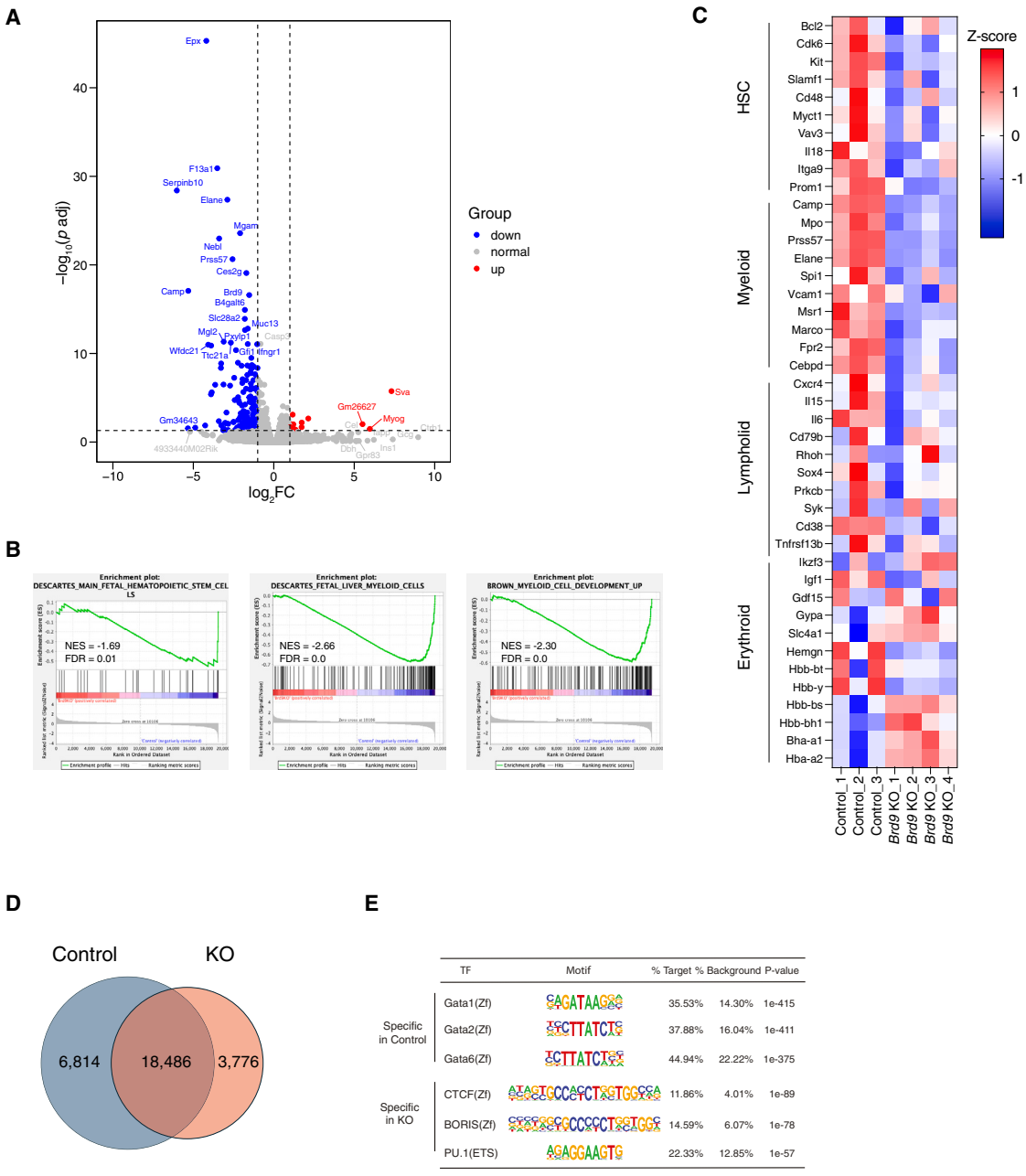

Figure 3. *Brd9* KO altered chromatin state and transcription, leading to disturbed HSC and myeloid program

(A) Volcano plot of differential mRNA expression in *Brd9* KO group ($n = 4$ fetuses), compared with control group ($n = 3$ fetuses) in E14.5 FL Lin$^-$. Upregulated genes in *Brd9* KO are highlighted in red and downregulated ones in blue, applying adjusted $p < 0.05$ and $|\log_2 FC| > 1$. The x axis represents $\log_2$ fold change (FC) values, the y axis represents -$\log_{10}$ of adjusted p values.

(B) GSEA enrichment plot for dysregulated genes in RNA-seq of *Brd9* KO vs. control. NES: normalized enrichment score, FDR: false discovery rate.

(C) Heatmap showing the expression (Z scores) of the representative genes related to HSC, myeloid, lymphoid and erythroid development on control and *Brd9* KO.

(D) The genomic overlap of ATAC-seq peaks from control and *Brd9* KO. $n = 1$ for each group.

(E) Transcriptional factor motif analysis of comparing specific ATAC-seq peaks between control and *Brd9* KO groups. The p values were calculated using binomial distribution in HOMER.

SWI/SNF complexes, we speculated that BRD9 loss in FL cells may reduce chromatin accessibility, leading to transcriptional repression. To investigate the hypothesis, ATAC-seq was performed using FL Lin$^-$c-Kit$^+$ cells from E14.5 *Brd9*$^{fl/fl}$ control and *Vav1*-iCre; *Brd9*$^{fl/fl}$ fetuses. While 18,486 peaks overlapped between the control and KO groups, the number of KO-specific peaks (3,776) was nearly half of that of control-specific peaks (6,814) (Figure 3D). Homer motif analysis[41] revealed erythroid

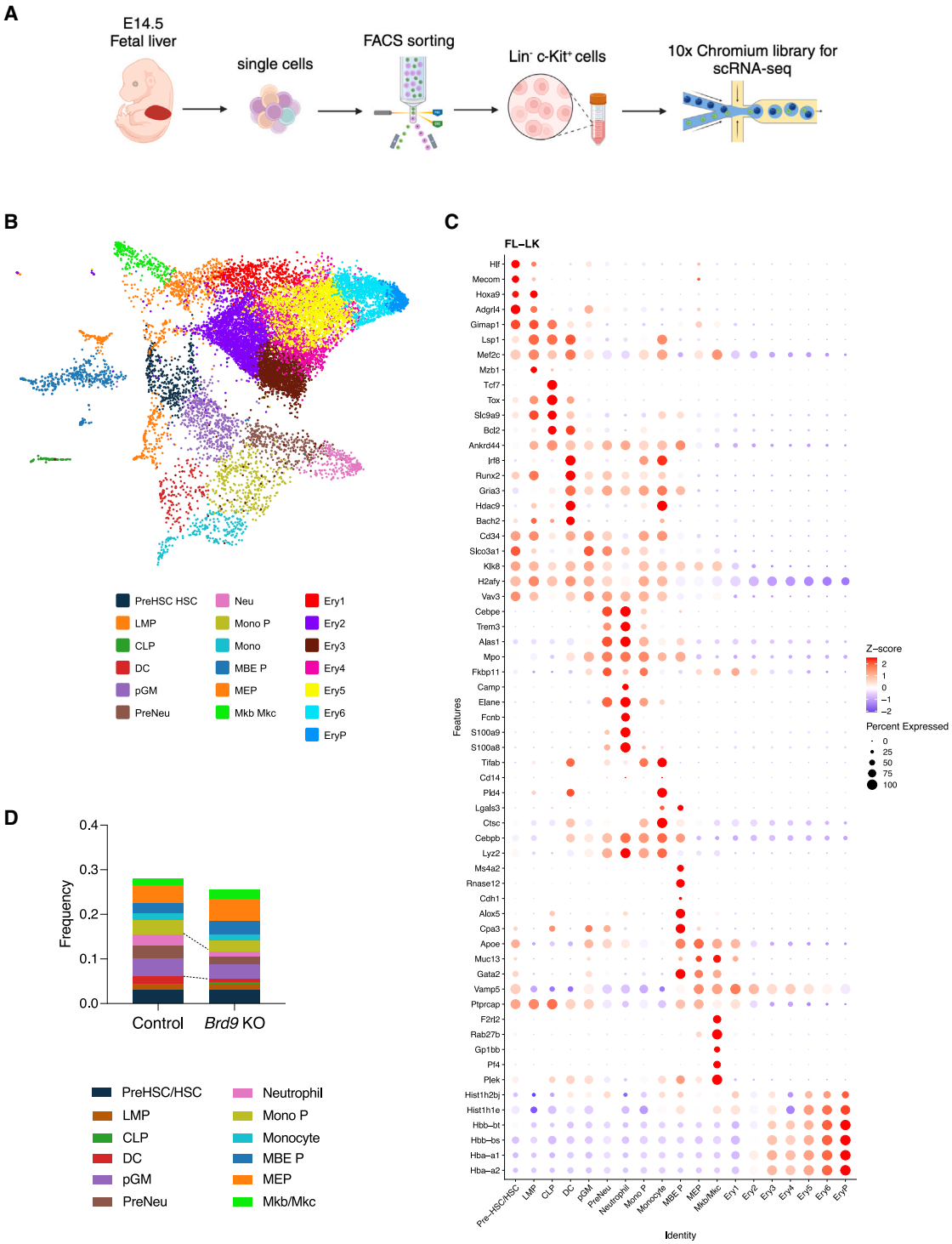

Figure 4. Characterization of *Brd9* KO FL cells at a single-cell level

(A) Schema of scRNA-seq experiment. E14.5 FL was harvested from control fetus or *Brd9* KO fetus and proceeded to single cell isolation. Lin⁻c-Kit⁺ (LK) cells were sorted by FACS sorter and proceeded to the 10 x Chromium library for scRNA-seq.

(B) Identification of distinct clusters based on uniform manifold approximation and projection (UMAP) plot containing 14,688 E14.5 FL LK cells from control and *Brd9* KO. The cell types were assigned based on the expression of hematopoietic lineage marker genes listed in (C). Abbreviation: LMP, lympho-myeloid progenitors; CLP, common lymphoid progenitors; DC, dendritic cells; pGM, pre-granulocyte/macrophage progenitors; PreNeu, neutrophil precursors;

(legend continued on next page)

GATA-related motifs (GATA1, GATA2, and GATA6) specifically detected in the control group, while CTCF-related motifs (CTCF and BORIS) were enriched in the *Brd9* KO group (Figure 3E). To ensure reproducibility, we performed a duplicate ATAC-seq using the same sampling strategy. The Homer motif analysis of the overlapping ATAC peaks within each group closely mirrored the results observed in the previous experiment (Figure S5E). In contrast to our findings that the ATAC signals of super-enhancers (SE) and typical enhancers (TE) were significantly increased in adult KO HSPCs,[22] the fetal KO counterparts displayed a modest alteration in ATAC signals at both SE and TE regions, as estimated by H3K27Ac signals[7] (Figure S5F). Collectively, in the FL, Loss of *Brd9* impairs pathways involved in myeloid differentiation and stemness, likely affected by reduced chromatin accessibility, and this occurs through mechanisms distinct from those observed in adult BM.

Characterization of *Brd9* KO FL cells at a single-cell level

To decipher the effects of *Brd9* deletion on lineage commitment identity and priming of HSPCs, we performed single-cell RNA-seq (scRNA-seq) targeting 10,000 $Lin^{-}c\text{-}Kit^{+}$ cells from control and KO E14.5 FL (Figure 4A). Uniform manifold approximation and projection (UMAP) analysis integrating both models revealed the expected stem and progenitor clusters, including first definitive hematopoietic stem cells (preHSC/HSC), lympho-myeloid progenitors (LMP), CLP, dendritic cells (DC), pre-granulocyte/macrophage progenitors (pGM), neutrophil precursors (PreNeu), neutrophils (Neu), monocyte precursors (Mono P), monocytes (Mono), mast cell/basophil/eosinophil progenitors (MBE P), megakaryocyte-erythroid progenitors (MEP), megakaryoblasts/megakaryocytes (Mkb/Mkc), erythroid cells (Ery1-6), primitive erythrocytes (EryP)[42,43] (Figure 4B). Representative gene markers shown in Figure 4C were used to define and distinguish cell populations (Table S1).[42,43] Notably, stemness-related genes such as *Hlf*, *Mecom*, *Hoxa9*, *Adgr4*, and *Gimap1* were used to define PreHSC/HSC. Given our interest in myeloid-related phenotypes, myeloid progenitors were defined as pGM (high expression of *Cd34*, *Slco3a1*, *Klk8*, *H2afy*, and *Vav3*) and PreNeu (high expression of *Cebpe*, *Trem3*, *Alas1*, *Mpo*, and *Fkbp11*). Genes expressed in mature neutrophils such as *Camp*, *Elane*, *Fcnb*, *S100a9*, and *S100a8* were used to define neutrophil (Neu) population. In line with the bulk RNA-seq analysis (Figures 3A–3C), which indicated the downregulation of myeloid-associated genes, the frequencies of the pGM, PreNeu, and Neu fraction robustly decreased in the KO group, as shown in Figure 4D.

Brd9 KO determines the cell fate of HSPCs in FL

As for the detailed investigation into each fraction, we first noticed that myeloid progenitors (pGM, PreNeu, and Neu) were less abundant in the *Brd9* KO group, as shown in the highlighted UMAP (Figures 5A and 4D). We calculated DEGs in each progenitor fraction and discovered links between DEGs and specific pathways. For example, DEGs downregulated in KO PreNeu were enriched in myeloid-related pathways, such as neutrophil degranulation, and involved TFs essential for myeloid development, including MYB, MYC, TAL1, BRD4, MECOM, and SPI1 (Figure 5B). To further understand the cell fate of myeloid progenitors in the *Brd9* KO, we utilized CellRadar[44] analysis of DEGs upregulated in control and KO PreNeu/pGM. As shown in Figure 5C, while control PreNeu and pGM were more restricted toward preGM and GMP, *Brd9* KO cells lacked clear direction in myeloid differentiation. Detailed examination of scRNA-seq data revealed significant downregulation of key myeloid markers such as *Elane*, *Ccl9*,[45] and *Prss57*[38] in KO PreNeu (Figure 5D). Regarding erythroid progenitors, we focused on the mechanism underlying the maturation disturbance (Figure 1F). The KO sample displayed an increase in early-stage progenitors (Ery2 and Ery3) and a reciprocal decrease in later-stage progenitors (Ery6 and EryP), indicating a maturation block in the middle of the process (Figure 5E). Genes involved in later erythroblast stages, such as *Hemgn*[46,47] and *Hbb-bt*, were downregulated in *Brd9* KO (Figure 5F). In the CellRadar analysis, we discovered that upregulated DEGs from total erythroid-lineage cells (Ery1-6 and EryP) in the KO group exhibited fewer characteristics of CFU-E (Figure 5G). These findings from scRNA-seq further connect the phenotypic alterations in myeloid and erythroid lineages with transcriptional changes at a single-cell level, elucidating the broad impact of BRD9 loss on hematopoietic differentiation.

BRD9 behaves oppositely in the myeloid differentiation of fetal HSPCs compared to adult HSPCs

We have elucidated the broad impact of BRD9 loss on hematopoietic differentiation in FL so far. Our next question is what difference BRD9 loss makes on hematopoiesis in FL and adult BM. To show the discrepant results on phenotypes between KO FL and KO adult BM, we integrated four scRNA-seq data (control/KO FL HSPCs and previously deposited control/KO adult BM HSPCs[22]) and compared four groups in the UMAP analysis (Figure 6A). We also conducted RNA velocity analysis using cellDancer[48] to infer cellular state transitions by evaluating the transcription dynamics of premature (unspliced) and mature (spliced) mRNA, and cell velocities were superimposed on the UMAP space (Figure 6B). Although RNA velocity analysis indicates that the directional flows toward each lineage were preserved under *Brd9* KO conditions in both the FL and adult BM, the cellular fractions of specific cell types were altered. Compared to adult BM HSPCs, FL HSPCs are more committed to erythroid lineage with fewer myeloid or lymphoid progenitors, consistent with the fetus's need for more red blood cells to support rapid development[49] (Figure 6A). As we previously reported,[22] in *Brd9* KO adult BM, the frequency of

Neu, neutrophils; mono P, monocyte precursors; MBE P, Mast cell/basophil/eosinophil progenitors; MEP, megakaryocyte-erythroid progenitors; Ery1-6, erythroid cells; EryP, primitive erythrocytes.

(C) Dot plot showing the average expression of selected marker genes in each hematopoietic cluster. The size of dots represents the fraction of cells expressing a given gene. The cluster-wise mean expression value is shown by *Z* score and dots are colored based on this value.

(D) The cellular frequency of non-erythroid clusters in control and *Brd9* KO groups. Dash lines display myeloid population change between control and *Brd9* KO.

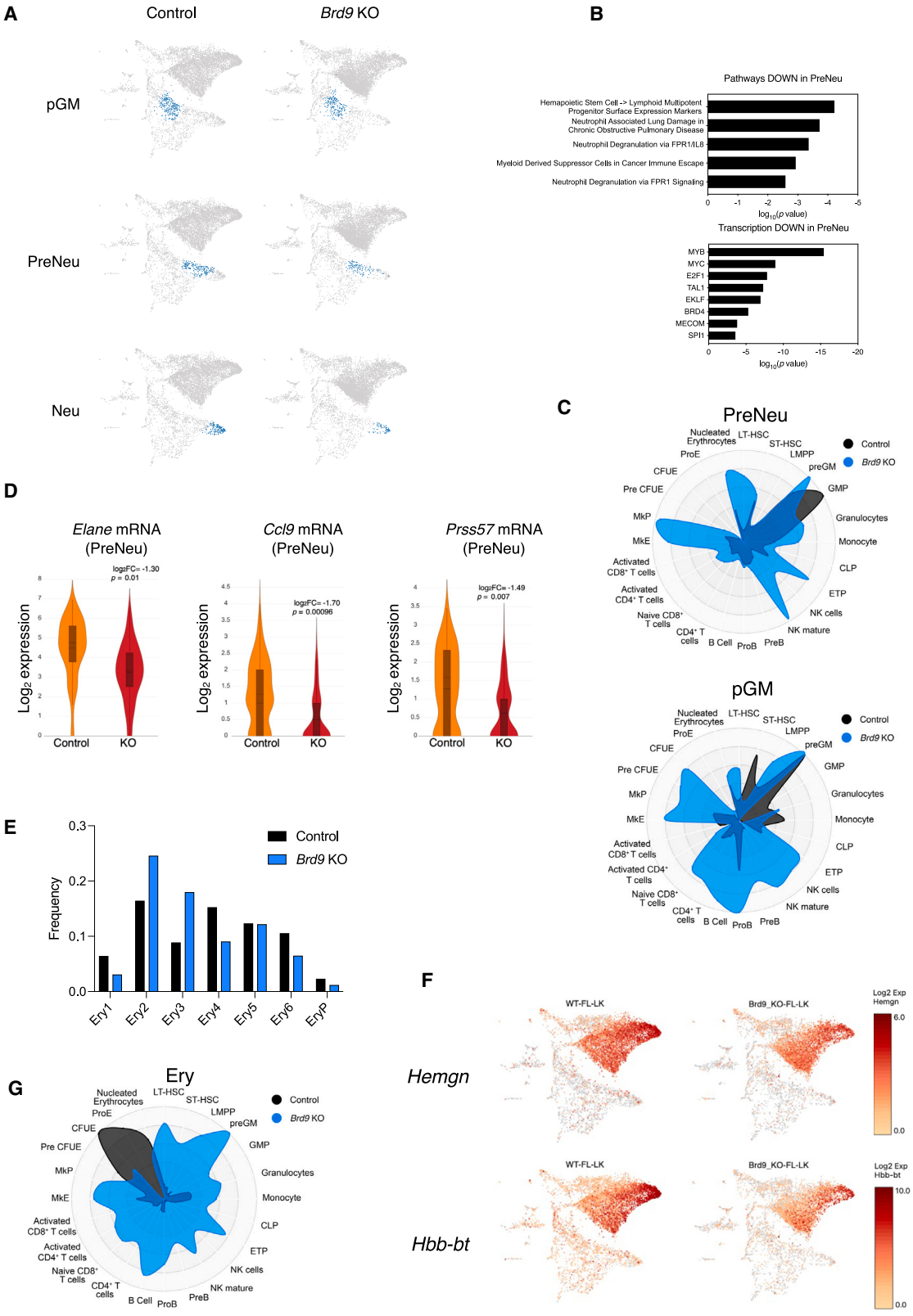

(legend on next page)

transcriptionally-defined PreHSC/HSCs and erythroid-committed progenitors were reduced, while the myeloid-committed progenitors increased, compared to control adult BM[22] (Figure 6A). However, most of these changes were not reproduced in the *Brd9* KO FL: the disturbance in erythroid maturation was relatively modest, and myeloid maturation was weakened in the *Brd9* KO FL (Figure 6A). Specifically, the number of cells along the differentiation velocities toward the myeloid lineage decreased in the *Brd9* KO FL compared to the control FL, particularly among the pGM, PreNeu, and neutrophil fractions (Figure 6B). Overall, the scRNA-seq data were consistent with the phenotypes observed *in vivo* (Figure 1 and Xiao et al; [22]) and highlighted a discrepancy in myeloid development between FL and adult BM. This is further corroborated by flowcytometric analysis, which showed a reduced CMP ($CD34^{+}Fc\gamma R^{-}$ LK) frequency in KO FL, in contrast to an increased CMP frequency in KO BM (Figure 6C).

Given that BRD9 is a pivotal chromatin regulator at least for adult hematopoiesis,[22] we compared control vs. KO ATAC-seq data in adult BM and FL to reveal the differential effects of BRD9 loss on chromatin states. Contrary to the reduction of ATAC peaks observed in biologically replicated FL samples (Figures 3D, 6D, and S5E), we reported enhanced ATAC peaks in KO adult BM when compared to control adult BM.[22] Thus, altered ATAC-seq peaks in each comparison (control vs. KO FL and control vs. KO adult BM) were subjected to GREAT analysis[50] to investigate the affected pathways. Notably, the pathways enriched at closed chromatin in *Brd9* KO FL were discrepantly found in those at open chromatin in KO BM, including pathways related to erythropoiesis, myeloid development, and activation (Figure 6E). These findings were consistent with the suppressed and enhanced peaks located at neighboring myeloid-associated genes, such as *Spi1*, *Itgam*, and *Fcna* in KO FL and KO BM, respectively (Figures 6F, S6A, and S6B). Collectively, BRD9 deletion differentially alters the cell fate of HSPCs between FL and adult BM. Specifically, myeloid differentiation was impeded in *Brd9* KO FL but accelerated in *Brd9* KO adult BM, highlighting the unique and context-dependent effects of BRD9 on chromatin regulation.

To investigate the mechanism underlying the differential effects of BRD9 in fetal versus adult hematopoiesis, we integrated current RNA/ATAC data with publicly available three-dimensional genome folding data in fetal and adult wild-type HSCs (e.g., enhancer-promoter (EP) loops, Chen et al.[8]). This resource demonstrated how dynamic EP interactions contribute to phenotypic differences between FL (E14.5) and adult BM HSCs through the analysis of H3K27Ac/H3K4me1 ChIP-seq, ATAC-seq, and Capture-C methods, identifying FL- and BM-specific EP interactions. Given that upregulated genes were predominant in *Brd9* KO BM cells,[22] while downregulated genes were more prevalent in *Brd9* KO FL cells, we integrated DEGs in adult and fetal *Brd9* KO HSCs with the reported FL- or BM-specific EP loops in a wild-type background. This analysis led to the identification of EP loop-associated DEGs (EP-DEGs) specific to *Brd9* KO in BM or FL (Figures S7A and S7B). Notably, the FL-specific downregulated EP-DEGs (89 genes) were significantly enriched for the pathways and TFs involved in myeloid development.

Furthermore, previous studies, including ours,[16,17,22,51] have shown that BRD9 colocalizes with CTCF. Given that CTCF binding has been reported to both promote and repress gene expression by functioning as a genomic insulator,[52,53] we speculate that *Brd9* KO may regulate the fundamental chromatin looping via CTCF, modulating EP interactions and constructing specific gene networks in a context-dependent, FL- and BM-specific manner. To explore this, we examined the differential ATAC peaks caused by *Brd9* KO of ±100 kb from the transcription start site (TSS) of EP-DEGs in FL and BM (Figure S7). In *Brd9* KO FL, the predominantly closed ATAC peaks associated with downregulated EP-DEG were enriched for GATA family motifs, which is consistent with the disrupted phenotypes of HSPC and myeloid/erythroid lineage (Figures S7A and 1D–1H). Conversely, in KO BM, the opened ATAC peaks associated with upregulated EP-DEGs were enriched for myeloid/erythroid-related motifs, including Fli1 and PU.1, as we previously reported (Figure S7B).[22] Interestingly, despite the opposite effects of *Brd9* KO on global gene expression, both *Brd9* KO FL and BM exhibited enrichment of the CTCF motif in ATAC peaks associated with EP-DEGs (Figures S7A and S7B).

DISCUSSION

Our current study elucidates the pivotal roles of BRD9 in fetal hematopoiesis, with a detailed comparative analysis against adult hematopoiesis. We focused on the E14.5 developmental stage in the fetus, a critical period when HSCs are at their peak in the FL,[28] and *Vav1*-driven iCre recombinase is optimally expressed to facilitate *Brd9* deletion.[25–27] *Brd9* KO resulted in a pronounced impairment of myeloid development in the fetus, as evidenced by diminished myeloid colony-forming capacity and the downregulation of key myeloid-related genes. Notably, several essential genes involved in myeloid differentiation, including *Elane*, *Camp*, and *Mpo*, exhibited significant downregulation in KO models (Figure S5C). Our integrated analysis of RNA-seq and ATAC-seq revealed fetal-specific dynamics in transcription and

Figure 5. *Brd9* KO determines the cell fate of HSPCs in FL

(A) The estimated myeloid progenitor clusters (pGM, PreNeu, and Neu) are highlighted in UMAP between control and *Brd9* KO groups.

(B) Enrichr pathway analysis shows downregulated pathways and transcription factors in PreNeu cluster, compared between control and *Brd9* KO group.

(C) CellRadar plots of upregulated DEGs between control and *Brd9* KO in PreNeu and pGM.

(D) The violin plots of myeloid-related genes (*Elane*, *Ccl9*, and *Prss57*) mRNA expression in the indicated cluster, where 209 and 129 cells belong to control and *Brd9* KO, respectively. Boxplot and kernel density plot of $\log_2$ expression values are shown. The *p* values were obtained by negative binomial test and adjusted using the Benjamini-Hochberg correction. In the box-and-whisker plots, the 0th, 25th, 50th, 75th, and 100th percentiles and mean (dashed lines) are shown.

(E) The estimated cellular frequency in erythroid clusters in control and *Brd9* KO groups.

(F) The expression of the genes related to erythroid maturation (*Hemgn* and *Hbb-bt*) is shown to display the difference of FL clusters between control and *Brd9* KO.

(G) CellRadar plots of upregulated DEGs between control and *Brd9* KO in erythroid cells (Ery1-6 and EryP).

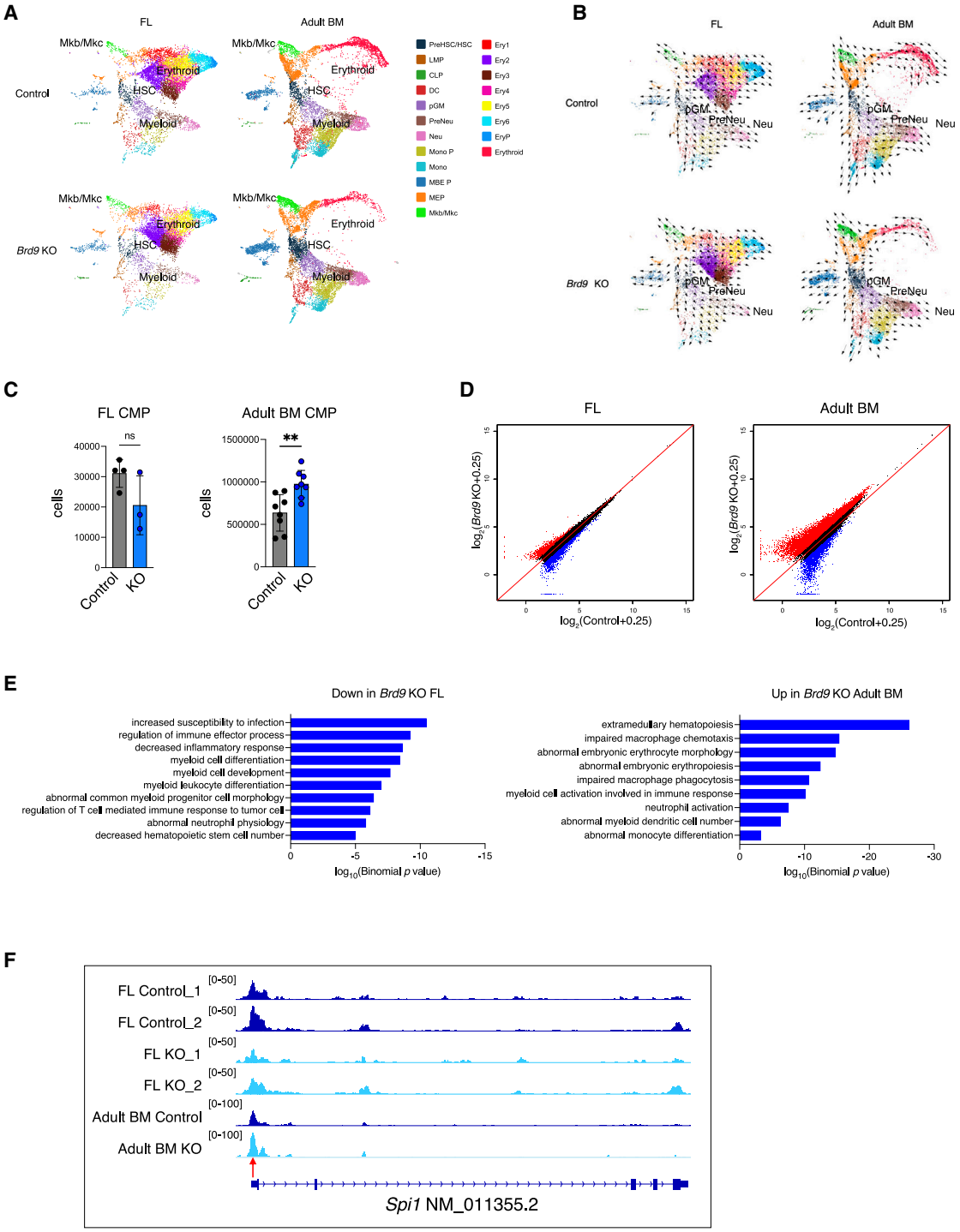

Figure 6. BRD9 behaves oppositely in the myeloid differentiation of fetal HSPCs compared to adult HSPCs

(A) Identification of hematopoietic clusters based on UMAP space displaying LK cells derived from E14.5 FL and Adult BM, grouped by control and *Brd9* KO.

(B) The cell velocities derived from CellDancer on cell types in E14.5 FL and Adult BM, grouped by control and *Brd9* KO.

(C) FACS analysis of common myeloid progenitors (CMP, CD34^{+}FcγR^{-} LK) derived from E14.5 FL and adult BM, grouped by control and *Brd9* KO, respectively. FL control $n = 4$ fetuses, FL *Brd9* KO $n = 3$ fetuses, Adult BM control $n = 8$ mice, Adult BM *Brd9* KO $n = 8$ mice independent experiments, data are represented as mean ± s.e.m. $^{**}p < 0.01$; ns, not significant ($p > 0.05$) The p value relative to control was calculated by two-tailed unpaired t-test.

(D) Scatterplots displaying differential ATAC-seq signals calculated by $\log_2$(ATAC-signal+0.25) between control and *Brd9* KO in FL and Adult BM. ATAC-seq signals of control and *Brd9* KO at consensus peaks from duplicated samples in FL were calculated by geometric mean. Each dot represents an individual peak in the unified peak set. The upregulated peaks (red) and the downregulated ones (blue) are determined with a fold-change threshold 1.5.

(legend continued on next page)

genome accessibility that were absent in adult BM. This aligns with previous reports indicating that chromatin state undergoes dynamic changes during the transition from fetal to adult stages.[8] For instance, a common BAF complex member *Smarca2* gains epigenetic modifications during this process, leading to higher expression in adult BM HSCs.[8] Further studies are warranted to elucidate the detailed mechanisms by which genomic and epigenomic networks switch from fetal to adult hematopoiesis.

In addressing the relative myeloid deficiency observed in *Brd9* KO fetuses, we extended our analysis to the earlier stage of HSPCs. *Brd9*-deficient fetal HSCs demonstrated diminished stem cell capacity (Figure 2C), consistent with the flow cytometric analysis showing reduced LT-HSC frequency in *Brd9 KO* FL. Specifically, we observed an increase in ST-HSCs in primary FL but a decrease in this fraction within engrafted FL cells (Figures 1D and 2D). Similarly, the MEP fraction showed an opposite trend in FACS analysis, suggesting that BRD9's context-dependent roles initiates before HSCs commit to MEPs. This necessitates further investigation into the differences between FL and adult BM environments, such as stem cell niches.

In addition to myeloid population disturbances, erythroid maturation is notably affected in *Brd9* KO FL cells. Analysis of erythroid progenitors, using CD71 and Ter-119 markers, revealed that *Brd9* KO leads to an increase in immature S1 and S2 fractions and a decrease in more differentiated S4 and S5 fractions (Figure 1E). This trend was corroborated by scRNA-seq data (Figure 5E). Intriguingly, genes associated with hemoglobin production were significantly impacted by *Brd9* deletion. RNA-seq analysis showed upregulation of adult-type hemoglobin genes (*Hbb-bs*, *Hbb-bh1*, *Hba-a1*, *Hba-a2*) and downregulation of fetal-type hemoglobin genes (*Hbb-*γ) in *Brd9* KO models (Figure 3C). This is consistent with previous studies indicating that the transition from fetal to adult hemoglobin, occurring between E11.5 and E13.5 in mice, is regulated by various TFs, such as GATA1, NFE2, KLF1, and TAL1.[54,55] GATA1, for instance, has been shown to recruit BRG1 and the BAF complex to drive epigenetic alterations, thereby regulating erythroid differentiation.[19] Considering BRG1 is a common member of entire BAF complex,[56] the specific involvement of BRD9, a unique member of the ncBAF complex,[21] in this process remains to be elucidated. To gain deeper insights into BRD9's differential roles between FL and adult BM HSCs, we conducted an integrated analysis of RNA-seq, ATAC-seq (Figure 3) and previously described FL- and BM-specific enhancer-promoter (EP) loop data.[8] As shown in Figure S7, we speculate that BRD9 regulates essential gene networks involved in differentiation in a context-dependent manner, specific to either FL or BM (Figure S7). While the BRD9-CTCF-mediated EP loop emerged as a shared mechanism for reshaping chromatin three-dimensional landscapes, further investigation is required to fully comprehend the transition from FL to BM hematopoiesis.

In summary, our research underscores the critical role of BRD9 in fetal hematopoiesis. *Brd9* deficiency not only compromises FL HSC stemness and myeloid development but also disrupts erythroid maturation. The differential roles of BRD9 in fetal versus adult hematopoiesis highlight the necessity of establishing a distinct framework for fetal hematopoiesis to enhance our understanding of pediatric blood diseases. Future investigations should aim to delineate the heterogeneous components of hematopoiesis and context-dependent roles of chromatin regulators.

Limitations of the study

Our findings indicate a shared impairment of HSCs in both FL and BM, along with differential effects of BRD9 on myeloid progenitor commitment between these two environments. It is still uncertain whether the distinct behavior of BRD9 arises from variations in its chromatin binding and cooperative partners or from differences in the hematopoietic microenvironment. While we have conducted extensive analysis of chromatin accessibility and transcriptomics at the single-cell level, the underlying mechanisms governing BRD9's direct involvement in each stage of myeloid differentiation remain to be elucidated. Additionally, the technical limitations of colony formation assays and the transplantation of FL cells into adult BM complicate the assessment of BRD9's direct role in lineage commitment and terminal differentiation in the FL, particularly given the scarcity of mature myeloid cells. Employing detailed lineage tracing with barcoding systems and fluorescent reporter systems could provide valuable insights and alternative perspectives to enhance our understanding of these processes. For the HSPC analysis, we did not differentiate between male and female fetuses. Consequently, this study cannot rule out the potential influence of sex on the observed outcomes.

RESOURCE AVAILABILITY

Lead contact

Requests for further information should be directed to and will be fulfilled by the lead contact, Daichi Inoue d-inoue@patho.med.osaka-u.ac.jp).

Materials availability

This study did not generate new unique reagents. All materials used in this study will be made freely available upon request and the completion of applicable material transfer agreements. The information about reagents or other materials are provided in the key resources table.

Data and code availability

- Sequencing data generated in this study have been deposited in the Gene Expression Omnibus (GEO): GSE269210 (RNA-seq, scRNA-seq, ATAC-seq). This is also provided in the key resources table.
- This paper does not report the original code.
- Data reported in this paper will be shared by the lead contact upon request.

ACKNOWLEDGMENTS

We thank Foundation for Biomedical Research and Innovation at Kobe (FBRI). We thank Facility for iPS Cell Therapy, CiRA Foundation to collaborate on scRNA-seq. This work was supported by JST SPRING (grant number

(E) GREAT analysis processing ATAC-seq peaks in each group shows representative downregulated pathways in *Brd9* KO FL and upregulated pathways in *Brd9* KO adult BM.

(F) Coverage tracks showing ATAC-seq reads around *Spi1* gene locus between E14.5 FL and Adult BM, grouped by control and *Brd9* KO. The arrow indicates differentially altered ATAC peaks by *Brd9* KO between FL and adult BM.

JPMJSP2110 to Y.Z.), JSPS KAKENHI (JP24H00866 to D.I., JP20H00537 to D.I., JP23H00430 to D.I., JP24K21298 to D.I., and JP23K07824 to K.N.), JST CREST (JPMJCR23B7 to D.I.), AMED (JP23ck0106697, JP23gm6210022, JP24ama221126 to D.I., and JP24ama221135 to K.N.), Japanese Society of Hematology (to D.I.), The Naito Foundation (to D.I. and K.N.), Ono Pharmaceutical Foundation for Oncology (to D.I.), The Mitsubishi Foundation (to D.I.), Takeda Science Foundation (to D.I. and K.N.), The Sumitomo Foundation (to D.I.), The Uehara Memorial Foundation (to D.I.), Princess Takamatsu Cancer Research Fund (to D.I., and K.N.), Kobayashi Foundation for Cancer Research (to D.I.), Friends of Leukemia Research Fund (to K.N.), Mochida Memorial Foundation for Medical and Pharmaceutical Research (to K.N.), MSD Life Science Foundation, Public Interest Incorporated Foundation (to K.N.) and The Cell Science Research Foundation (to D.I.). The scheme figures in Main Figure 1A, 2A, and 4A and Graphical Abstract were produced with Biorender.

AUTHOR CONTRIBUTIONS

D.I., K.N., and Y.Z. designed the study. Y.Z., D.I., K.N., M.N., and H.Y. wrote the manuscript. Y.Z. and W.Z. performed bulk RNA-seq experiments and data analysis. Y.Z. and M.F. performed ATAC-seq experiments. Y.Z. and K.N. performed scRNA-seq experiments. M.N. and Y.Z. performed data analysis of ATAC-seq and scRNA-seq. Y.Z., Y.K., M.F., H.I., W.S., and C.H. performed animal experiments. M.X., A.T., and Y.A. provided suggestion and materials for the study. In revision experiments, W.S. and C.H. collected fetal liver hematopoietic cells and performed colony formation assay described in Figures 1G, 1H, and S2D–S2F. D.I. supervised the study.

DECLARATION OF INTERESTS

The authors declare no competing interests.

STAR★METHODS

Detailed methods are provided in the online version of this paper and include the following:

- KEY RESOURCES TABLE
- EXPERIMENTAL MODEL AND STUDY PARTICIPANT DETAILS
  - Animals
  - Generation of *Vav1*-iCre; *Brd9*$^{fl/fl}$ mice
- METHOD DETAILS
  - Isolation of mouse fetal liver, bone marrow and spleen cells
  - Flow cytometry, FACS sorting and Western blot analysis
  - Colony formation assay
  - I-BRD9 treatment
  - Retroviral transduction
  - Transplantation assay and limiting dilution assay
  - Bulk RNA-seq
  - ATAC-seq
  - Single cell RNA-seq library preparation
- QUANTIFICATION AND STATISTICAL ANALYSIS

SUPPLEMENTAL INFORMATION

Supplemental information can be found online at https://doi.org/10.1016/j.isci.2025.112010.

Received: July 18, 2024
Revised: October 19, 2024
Accepted: February 10, 2025
Published: February 12, 2025

REFERENCES

1. Laurenti, E., and Göttgens, B. (2018). From haematopoietic stem cells to complex differentiation landscapes. Nature *553*, 418–426. https://doi.org/10.1038/nature25022.
2. Haas, S., Trumpp, A., and Milsom, M.D. (2018). Causes and Consequences of Hematopoietic Stem Cell Heterogeneity. Cell Stem Cell *22*, 627–638. https://doi.org/10.1016/j.stem.2018.04.003.
3. Orfao, A., Matarraz, S., Pérez-Andrés, M., Almeida, J., Teodosio, C., Berkowska, M.A., and van Dongen, J.J.M.; EuroFlow (2019). Immunophenotypic dissection of normal hematopoiesis. J. Immunol. Methods *475*, 112684. https://doi.org/10.1016/j.jim.2019.112684.
4. Siminovitch, L., McCulloch, E.A., and Till, J.E. (1963). The Distribution of Colony-Forming Cells among Spleen Colonies. J. Cell. Comp. Physiol. *62*, 327–336. https://doi.org/10.1002/jcp.1030620313.
5. Ganuza, M., Clements, W., and McKinney-Freeman, S. (2022). Specification of hematopoietic stem cells in mammalian embryos: a rare or frequent event? Blood *140*, 309–320. https://doi.org/10.1182/blood.2020009839.
6. Canu, G., and Ruhrberg, C. (2021). First blood: the endothelial origins of hematopoietic progenitors. Angiogenesis *24*, 199–211. https://doi.org/10.1007/s10456-021-09783-9.
7. Yokomizo, T., Ideue, T., Morino-Koga, S., Tham, C.Y., Sato, T., Takeda, N., Kubota, Y., Kurokawa, M., Komatsu, N., Ogawa, M., et al. (2022). Independent origins of fetal liver haematopoietic stem and progenitor cells. Nature *609*, 779–784. https://doi.org/10.1038/s41586-022-05203-0.
8. Chen, C., Yu, W., Tober, J., Gao, P., He, B., Lee, K., Trieu, T., Blobel, G.A., Speck, N.A., and Tan, K. (2019). Spatial Genome Re-organization between Fetal and Adult Hematopoietic Stem Cells. Cell Rep. *29*, 4200–4211.e7. https://doi.org/10.1016/j.celrep.2019.11.065.
9. Narlikar, G.J., Sundaramoorthy, R., and Owen-Hughes, T. (2013). Mechanisms and functions of ATP-dependent chromatin-remodeling enzymes. Cell *154*, 490–503. https://doi.org/10.1016/j.cell.2013.07.011.
10. Lickert, H., Takeuchi, J.K., Von Both, I., Walls, J.R., McAuliffe, F., Adamson, S.L., Henkelman, R.M., Wrana, J.L., Rossant, J., and Bruneau, B.G. (2004). Baf60c is essential for function of BAF chromatin remodelling complexes in heart development. Nature *432*, 107–112. https://doi.org/10.1038/nature03071.
11. Priam, P., Krasteva, V., Rousseau, P., D'Angelo, G., Gaboury, L., Sauvageau, G., and Lessard, J.A. (2017). SMARCD2 subunit of SWI/SNF chromatin-remodeling complexes mediates granulopoiesis through a CEBPvarepsilon dependent mechanism. Nat. Genet. *49*, 753–764. https://doi.org/10.1038/ng.3812.
12. Witzel, M., Petersheim, D., Fan, Y., Bahrami, E., Racek, T., Rohlfs, M., Puchałka, J., Mertes, C., Gagneur, J., Ziegenhain, C., et al. (2017). Chromatin-remodeling factor SMARCD2 regulates transcriptional networks controlling differentiation of neutrophil granulocytes. Nat. Genet. *49*, 742–752. https://doi.org/10.1038/ng.3833.
13. Alpsoy, A., and Dykhuizen, E.C. (2018). Glioma tumor suppressor candidate region gene 1 (GLTSCR1) and its paralog GLTSCR1-like form SWI/SNF chromatin remodeling subcomplexes. J. Biol. Chem. *293*, 3892–3903. https://doi.org/10.1074/jbc.RA117.001065.
14. Kaeser, M.D., Aslanian, A., Dong, M.Q., Yates, J.R., 3rd, and Emerson, B.M. (2008). BRD7, a novel PBAF-specific SWI/SNF subunit, is required for target gene activation and repression in embryonic stem cells. J. Biol. Chem. *283*, 32254–32263. https://doi.org/10.1074/jbc.M806061200.
15. Kadoch, C., Hargreaves, D.C., Hodges, C., Elias, L., Ho, L., Ranish, J., and Crabtree, G.R. (2013). Proteomic and bioinformatic analysis of mammalian SWI/SNF complexes identifies extensive roles in human malignancy. Nat. Genet. *45*, 592–601. https://doi.org/10.1038/ng.2628.
16. Michel, B.C., D'Avino, A.R., Cassel, S.H., Mashtalir, N., McKenzie, Z.M., McBride, M.J., Valencia, A.M., Zhou, Q., Bocker, M., Soares, L.M.M., et al. (2018). A non-canonical SWI/SNF complex is a synthetic lethal target in cancers driven by BAF complex perturbation. Nat. Cell Biol. *20*, 1410–1420. https://doi.org/10.1038/s41556-018-0221-1.
17. Gatchalian, J., Malik, S., Ho, J., Lee, D.S., Kelso, T.W.R., Shokhirev, M.N., Dixon, J.R., and Hargreaves, D.C. (2018). A non-canonical BRD9-containing BAF chromatin remodeling complex regulates naive pluripotency in

mouse embryonic stem cells. Nat. Commun. *9*, 5139. https://doi.org/10.1038/s41467-018-07528-9.

18. Liu, L., Wan, X., Zhou, P., Zhou, X., Zhang, W., Hui, X., Yuan, X., Ding, X., Zhu, R., Meng, G., et al. (2018). The chromatin remodeling subunit Baf200 promotes normal hematopoiesis and inhibits leukemogenesis. J. Hematol. Oncol. *11*, 27. https://doi.org/10.1186/s13045-018-0567-7.
19. Guo, X., Zhao, Y., Kim, J., and Dean, A. (2022). Hemogen/BRG1 cooperativity modulates promoter and enhancer activation during erythropoiesis. Blood *139*, 3532–3545. https://doi.org/10.1182/blood.2021014308.
20. Krosl, J., Mamo, A., Chagraoui, J., Wilhelm, B.T., Girard, S., Louis, I., Lessard, J., Perreault, C., and Sauvageau, G. (2010). A mutant allele of the Swi/Snf member BAF250a determines the pool size of fetal liver hemopoietic stem cell populations. Blood *116*, 1678–1684. https://doi.org/10.1182/blood-2010-03-273862.
21. Wang, X., Wang, S., Troisi, E.C., Howard, T.P., Haswell, J.R., Wolf, B.K., Hawk, W.H., Ramos, P., Oberlick, E.M., Tzvetkov, E.P., et al. (2019). BRD9 defines a SWI/SNF sub-complex and constitutes a specific vulnerability in malignant rhabdoid tumors. Nat. Commun. *10*, 1881. https://doi.org/10.1038/s41467-019-09891-7.
22. Xiao, M., Kondo, S., Nomura, M., Kato, S., Nishimura, K., Zang, W., Zhang, Y., Akashi, T., Viny, A., Shigehiro, T., et al. (2023). BRD9 determines the cell fate of hematopoietic stem cells by regulating chromatin state. Nat. Commun. *14*, 8372. https://doi.org/10.1038/s41467-023-44081-6.
23. Inoue, D., Chew, G.L., Liu, B., Michel, B.C., Pangallo, J., D'Avino, A.R., Hitchman, T., North, K., Lee, S.C.W., Bitner, L., et al. (2019). Spliceosomal disruption of the non-canonical BAF complex in cancer. Nature *574*, 432–436. https://doi.org/10.1038/s41586-019-1646-9.
24. Inoue, D., and Abdel-Wahab, O. (2016). Modeling SF3B1 Mutations in Cancer: Advances, Challenges, and Opportunities. Cancer Cell *30*, 371–373. https://doi.org/10.1016/j.ccell.2016.08.013.
25. Valerio, D.G., Xu, H., Eisold, M.E., Woolthuis, C.M., Pandita, T.K., and Armstrong, S.A. (2017). Histone acetyltransferase activity of MOF is required for adult but not early fetal hematopoiesis in mice. Blood *129*, 48–59. https://doi.org/10.1182/blood-2016-05-714568.
26. Dzierzak, E., and Medvinsky, A. (1995). Mouse embryonic hematopoiesis. Trends Genet. *11*, 359–366. https://doi.org/10.1016/s0168-9525(00)89107-6.
27. Stadtfeld, M., and Graf, T. (2005). Assessing the role of hematopoietic plasticity for endothelial and hepatocyte development by non-invasive lineage tracing. Development *132*, 203–213. https://doi.org/10.1242/dev.01558.
28. Wolber, F.M., Leonard, E., Michael, S., Orschell-Traycoff, C.M., Yoder, M.C., and Srour, E.F. (2002). Roles of spleen and liver in development of the murine hematopoietic system. Exp. Hematol. *30*, 1010–1019. https://doi.org/10.1016/s0301-472x(02)00881-0.
29. Kiel, M.J., Yilmaz, O.H., Iwashita, T., Yilmaz, O.H., Terhorst, C., and Morrison, S.J. (2005). SLAM family receptors distinguish hematopoietic stem and progenitor cells and reveal endothelial niches for stem cells. Cell *121*, 1109–1121. https://doi.org/10.1016/j.cell.2005.05.026.
30. Oguro, H., Ding, L., and Morrison, S.J. (2013). SLAM family markers resolve functionally distinct subpopulations of hematopoietic stem cells and multipotent progenitors. Cell Stem Cell *13*, 102–116. https://doi.org/10.1016/j.stem.2013.05.014.
31. Rodriguez-Fraticelli, A.E., Wolock, S.L., Weinreb, C.S., Panero, R., Patel, S.H., Jankovic, M., Sun, J., Calogero, R.A., Klein, A.M., and Camargo, F.D. (2018). Clonal analysis of lineage fate in native haematopoiesis. Nature *553*, 212–216. https://doi.org/10.1038/nature25168.
32. Shim, Y.A., Campbell, T., Weliwitigoda, A., Dosanjh, M., and Johnson, P. (2020). Regulation of CD71(+)TER119(+) erythroid progenitor cells by CD45. Exp. Hematol. *86*, 53–66.e1. https://doi.org/10.1016/j.exphem.2020.05.005.
33. Hu, Y., and Smyth, G.K. (2009). ELDA: extreme limiting dilution analysis for comparing depleted and enriched populations in stem cell and other assays. J. Immunol. Methods *347*, 70–78. https://doi.org/10.1016/j.jim.2009.06.008.
34. da Hora, C.C., Schweiger, M.W., Wurdinger, T., and Tannous, B.A. (2019). Patient-Derived Glioma Models: From Patients to Dish to Animals. Cells *8*, 1177. https://doi.org/10.3390/cells8101177.
35. Wilson, N.K., Kent, D.G., Buettner, F., Shehata, M., Macaulay, I.C., Calero-Nieto, F.J., Sánchez Castillo, M., Oedekoven, C.A., Diamanti, E., Schulte, R., et al. (2015). Combined Single-Cell Functional and Gene Expression Analysis Resolves Heterogeneity within Stem Cell Populations. Cell Stem Cell *16*, 712–724. https://doi.org/10.1016/j.stem.2015.04.004.
36. Kosciuczuk, E.M., Lisowski, P., Jarczak, J., Strzalkowska, N., Jozwik, A., Horbanczuk, J., Krzyzewski, J., Zwierzchowski, L., and Bagnicka, E. (2012). Cathelicidins: family of antimicrobial peptides. A review. Mol. Biol. Rep. *39*, 10957–10970. https://doi.org/10.1007/s11033-012-1997-x.
37. Klebanoff, S.J. (2005). Myeloperoxidase: friend and foe. J. Leukoc. Biol. *77*, 598–625. https://doi.org/10.1189/jlb.1204697.
38. O'Leary, N.A., Wright, M.W., Brister, J.R., Ciufo, S., Haddad, D., McVeigh, R., Rajput, B., Robbertse, B., Smith-White, B., Ako-Adjei, D., et al. (2016). Reference sequence (RefSeq) database at NCBI: current status, taxonomic expansion, and functional annotation. Nucleic Acids Res. *44*, D733–D745. https://doi.org/10.1093/nar/gkv1189.
39. Belaaouaj, A., Kim, K.S., and Shapiro, S.D. (2000). Degradation of outer membrane protein A in Escherichia coli killing by neutrophil elastase. Science *289*, 1185–1188. https://doi.org/10.1126/science.289.5482.1185.
40. Oikawa, T., Yamada, T., Kihara-Negishi, F., Yamamoto, H., Kondoh, N., Hitomi, Y., and Hashimoto, Y. (1999). The role of Ets family transcription factor PU.1 in hematopoietic cell differentiation, proliferation and apoptosis. Cell Death Differ. *6*, 599–608. https://doi.org/10.1038/sj.cdd.4400534.
41. Heinz, S., Benner, C., Spann, N., Bertolino, E., Lin, Y.C., Laslo, P., Cheng, J.X., Murre, C., Singh, H., and Glass, C.K. (2010). Simple combinations of lineage-determining transcription factors prime cis-regulatory elements required for macrophage and B cell identities. Mol. Cell *38*, 576–589. https://doi.org/10.1016/j.molcel.2010.05.004.
42. Ceccacci, E., Villa, E., Santoro, F., Minucci, S., Ruhrberg, C., and Fantin, A. (2023). A Refined Single Cell Landscape of Haematopoiesis in the Mouse Foetal Liver. J. Dev. Biol. *11*, 15. https://doi.org/10.3390/jdb11020015.
43. Konturek-Ciesla, A., Dhapola, P., Zhang, Q., Säwén, P., Wan, H., Karlsson, G., and Bryder, D. (2023). Temporal multimodal single-cell profiling of native hematopoiesis illuminates altered differentiation trajectories with age. Cell Rep. *42*, 112304. https://doi.org/10.1016/j.celrep.2023.112304.
44. Bagger, F.O., Sasivarevic, D., Sohi, S.H., Laursen, L.G., Pundhir, S., Sønderby, C.K., Winther, O., Rapin, N., and Porse, B.T. (2016). BloodSpot: a database of gene expression profiles and transcriptional programs for healthy and malignant haematopoiesis. Nucleic Acids Res. *44*, D917–D924. https://doi.org/10.1093/nar/gkv1101.
45. Hara, T., Bacon, K.B., Cho, L.C., Yoshimura, A., Morikawa, Y., Copeland, N.G., Gilbert, D.J., Jenkins, N.A., Schall, T.J., and Miyajima, A. (1995). Molecular cloning and functional characterization of a novel member of the C-C chemokine family. J. Immunol. *155*, 5352–5358.
46. Dong, X.M., Zhao, K., Zheng, W.W., Xu, C.W., Zhang, M.J., Yin, R.H., Gao, R., Tang, L.J., Liu, J.F., Chen, H., et al. (2020). EDAG mediates Hsp70 nuclear localization in erythroblasts and rescues dyserythropoiesis in myelodysplastic syndrome. FASEB J. *34*, 8416–8427. https://doi.org/10.1096/fj.201902946R.
47. Zheng, W.W., Dong, X.M., Yin, R.H., Xu, F.F., Ning, H.M., Zhang, M.J., Xu, C.W., Yang, Y., Ding, Y.L., Wang, Z.D., et al. (2014). EDAG positively regulates erythroid differentiation and modifies GATA1 acetylation through recruiting p300. Stem Cell. *32*, 2278–2289. https://doi.org/10.1002/stem.1723.
48. Li, S., Zhang, P., Chen, W., Ye, L., Brannan, K.W., Le, N.T., Abe, J.I., Cooke, J.P., and Wang, G. (2024). A relay velocity model infers

cell-dependent RNA velocity. Nat. Biotechnol. *42*, 99–108. https://doi.org/10.1038/s41587-023-01728-5.

49. Palis, J., and Segel, G.B. (1998). Developmental biology of erythropoiesis. Blood Rev. *12*, 106–114. https://doi.org/10.1016/s0268-960x(98)90022-4.
50. McLean, C.Y., Bristor, D., Hiller, M., Clarke, S.L., Schaar, B.T., Lowe, C.B., Wenger, A.M., and Bejerano, G. (2010). GREAT improves functional interpretation of cis-regulatory regions. Nat. Biotechnol. *28*, 495–501. https://doi.org/10.1038/nbt.1630.
51. Alpsoy, A., Utturkar, S.M., Carter, B.C., Dhiman, A., Torregrosa-Allen, S.E., Currie, M.P., Elzey, B.D., and Dykhuizen, E.C. (2021). BRD9 Is a Critical Regulator of Androgen Receptor Signaling and Prostate Cancer Progression. Cancer Res. *81*, 820–833. https://doi.org/10.1158/0008-5472.CAN-20-1417.
52. Huang, H., Zhu, Q., Jussila, A., Han, Y., Bintu, B., Kern, C., Conte, M., Zhang, Y., Bianco, S., Chiariello, A.M., et al. (2021). CTCF mediates dosage- and sequence-context-dependent transcriptional insulation by forming local chromatin domains. Nat. Genet. *53*, 1064–1074. https://doi.org/10.1038/s41588-021-00863-6.
53. Kubo, N., Ishii, H., Xiong, X., Bianco, S., Meitinger, F., Hu, R., Hocker, J.D., Conte, M., Gorkin, D., Yu, M., et al. (2021). Promoter-proximal CTCF binding promotes distal enhancer-dependent gene activation. Nat. Struct. Mol. Biol. *28*, 152–161. https://doi.org/10.1038/s41594-020-00539-5.
54. Wang, X., and Thein, S.L. (2018). Switching from fetal to adult hemoglobin. Nat. Genet. *50*, 478–480. https://doi.org/10.1038/s41588-018-0094-z.
55. Kang, Y., Kim, Y.W., Yun, J., Shin, J., and Kim, A. (2015). KLF1 stabilizes GATA-1 and TAL1 occupancy in the human beta-globin locus. Biochim. Biophys. Acta *1849*, 282–289. https://doi.org/10.1016/j.bbagrm.2014.12.010.
56. Wong, A.K., Shanahan, F., Chen, Y., Lian, L., Ha, P., Hendricks, K., Ghaffari, S., Iliev, D., Penn, B., Woodland, A.M., et al. (2000). BRG1, a component of the SWI-SNF complex, is mutated in multiple human tumor cell lines. Cancer Res. *60*, 6171–6177.
57. Kim, D., Paggi, J.M., Park, C., Bennett, C., and Salzberg, S.L. (2019). Graph-based genome alignment and genotyping with HISAT2 and HISAT-genotype. Nat. Biotechnol. *37*, 907–915. https://doi.org/10.1038/s41587-019-0201-4.
58. Liao, Y., Smyth, G.K., and Shi, W. (2014). featureCounts: an efficient general purpose program for assigning sequence reads to genomic features. Bioinformatics *30*, 923–930. https://doi.org/10.1093/bioinformatics/btt656.
59. McCarthy, D.J., Chen, Y., and Smyth, G.K. (2012). Differential expression analysis of multifactor RNA-Seq experiments with respect to biological variation. Nucleic Acids Res. *40*, 4288–4297. https://doi.org/10.1093/nar/gks042.
60. Love, M.I., Huber, W., and Anders, S. (2014). Moderated estimation of fold change and dispersion for RNA-seq data with DESeq2. Genome Biol. *15*, 550. https://doi.org/10.1186/s13059-014-0550-8.
61. Chen, E.Y., Tan, C.M., Kou, Y., Duan, Q., Wang, Z., Meirelles, G.V., Clark, N.R., and Ma'ayan, A. (2013). Enrichr: interactive and collaborative HTML5 gene list enrichment analysis tool. BMC Bioinf. *14*, 128. https://doi.org/10.1186/1471-2105-14-128.
62. Kuleshov, M.V., Jones, M.R., Rouillard, A.D., Fernandez, N.F., Duan, Q., Wang, Z., Koplev, S., Jenkins, S.L., Jagodnik, K.M., Lachmann, A., et al. (2016). Enrichr: a comprehensive gene set enrichment analysis web server 2016 update. Nucleic Acids Res. *44*, W90–W97. https://doi.org/10.1093/nar/gkw377.
63. Xie, Z., Bailey, A., Kuleshov, M.V., Clarke, D.J.B., Evangelista, J.E., Jenkins, S.L., Lachmann, A., Wojciechowicz, M.L., Kropiwnicki, E., Jagodnik, K.M., et al. (2021). Gene Set Knowledge Discovery with Enrichr. Curr. Protoc. *1*, e90. https://doi.org/10.1002/cpz1.90.
64. Mootha, V.K., Lindgren, C.M., Eriksson, K.F., Subramanian, A., Sihag, S., Lehar, J., Puigserver, P., Carlsson, E., Ridderstråle, M., Laurila, E., et al. (2003). PGC-1alpha-responsive genes involved in oxidative phosphorylation are coordinately downregulated in human diabetes. Nat. Genet. *34*, 267–273. https://doi.org/10.1038/ng1180.
65. Subramanian, A., Tamayo, P., Mootha, V.K., Mukherjee, S., Ebert, B.L., Gillette, M.A., Paulovich, A., Pomeroy, S.L., Golub, T.R., Lander, E.S., and Mesirov, J.P. (2005). Gene set enrichment analysis: a knowledge-based approach for interpreting genome-wide expression profiles. Proc. Natl. Acad. Sci. USA *102*, 15545–15550. https://doi.org/10.1073/pnas.0506580102.
66. Bolger, A.M., Lohse, M., and Usadel, B. (2014). Trimmomatic: a flexible trimmer for Illumina sequence data. Bioinformatics *30*, 2114–2120. https://doi.org/10.1093/bioinformatics/btu170.
67. Langmead, B., and Salzberg, S.L. (2012). Fast gapped-read alignment with Bowtie 2. Nat. Methods *9*, 357–359. https://doi.org/10.1038/nmeth.1923.
68. Ramirez, F., Ryan, D.P., Gruning, B., Bhardwaj, V., Kilpert, F., Richter, A.S., Heyne, S., Dundar, F., and Manke, T. (2016). deepTools2: a next generation web server for deep-sequencing data analysis. Nucleic Acids Res. *44*, W160–W165. https://doi.org/10.1093/nar/gkw257.
69. Zhang, Y., Liu, T., Meyer, C.A., Eeckhoute, J., Johnson, D.S., Bernstein, B.E., Nusbaum, C., Myers, R.M., Brown, M., Li, W., and Liu, X.S. (2008). Model-based analysis of ChIP-Seq (MACS). Genome Biol. *9*, R137. https://doi.org/10.1186/gb-2008-9-9-r137.
70. Robinson, J.T., Thorvaldsdóttir, H., Winckler, W., Guttman, M., Lander, E.S., Getz, G., and Mesirov, J.P. (2011). Integrative genomics viewer. Nat. Biotechnol. *29*, 24–26. https://doi.org/10.1038/nbt.1754.
71. Hao, Y., Stuart, T., Kowalski, M.H., Choudhary, S., Hoffman, P., Hartman, A., Srivastava, A., Molla, G., Madad, S., Fernandez-Granda, C., and Satija, R. (2024). Dictionary learning for integrative, multimodal and scalable single-cell analysis. Nat. Biotechnol. *42*, 293–304. https://doi.org/10.1038/s41587-023-01767-y.
72. La Manno, G., Soldatov, R., Zeisel, A., Braun, E., Hochgerner, H., Petukhov, V., Lidschreiber, K., Kastriti, M.E., Lönnerberg, P., Furlan, A., et al. (2018). RNA velocity of single cells. Nature *560*, 494–498. https://doi.org/10.1038/s41586-018-0414-6.
73. Bergen, V., Lange, M., Peidli, S., Wolf, F.A., and Theis, F.J. (2020). Generalizing RNA velocity to transient cell states through dynamical modeling. Nat. Biotechnol. *38*, 1408–1414. https://doi.org/10.1038/s41587-020-0591-3.
74. Kay, M., Elkin, L. A., Higgins, J. J., and Wobbrock, J. O. (2021). ARTool: Aligned Rank Transform for Nonparametric Factorial ANOVAs. Zenodo, https://doi.org/10.5281/zenodo.594511.

STAR★METHODS

KEY RESOURCES TABLE

REAGENT or RESOURCE	SOURCE	IDENTIFIER
Antibodies		
Anti-CD3ε (Clone 145-2C11, conjugated to Biotin)	BioLegend	Cat#100304; RRID: AB_312669
Anti-CD4 (Clone GK1.5, conjugated to Biotin)	BioLegend	Cat#100404; RRID: AB_312689
Anti-CD8a (Clone 53-6.7, conjugated to Biotin)	BioLegend	Cat#100704; RRID: AB_312743
Anti-CD19 (Clone 6D5, conjugated to Biotin)	BioLegend	Cat#115504; RRID: AB_313639
Anti-NK1.1 (Clone PK136, conjugated to Biotin)	BioLegend	Cat#108704; RRID: AB_313391
Anti-Gr-1 (Clone RB6-8C5, conjugated to Biotin)	BD Pharmingen	Cat#51-01212J; RRID: AB_10053179
Anti-Ter-119 (Clone TER-119, conjugated to Biotin)	BD Pharmingen	Cat#51-09082J; RRID: AB_10053179
Anti-Ter-119 (Clone TER-119, conjugated to APC-Cy7)	BD Pharmingen	Cat#560509; RRID: AB_1645230
Anti-CD48 (Clone HM48-1, conjugated to APC-Cy7)	BioLegend	Cat#103432; RRID: AB_2561463
Anti-IL7r (Clone A7R34, conjugated to APC-Cy7)	BioLegend	Cat#135040; RRID: AB_2566161
Anti-CD3ε (Clone 145-2C11, conjugated to APC-Cy7)	BioLegend	Cat#100330; RRID: AB_1877170
Anti-Gr-1 (Clone RB6-8C5, conjugated to APC)	BD Pharmingen	Cat#553129; RRID: AB_398532
Anti-c-Kit (Clone 2B8, conjugated to APC)	BD Pharmingen	Cat#553356; RRID: AB_398536
Anti-B220 (Clone RA3-6B2, conjugated to PE/Cyanine7)	BioLegend	Cat#103222; RRID: AB_313005
Anti-Sca-1 (Clone D7, conjugated to PE/Cyanine7)	BioLegend	Cat#108114; RRID: AB_493596
Anti-Streptavidin (conjugated to PerCP/Cyanine5.5)	BioLegend	Cat#405214
Anti-CD11b (Clone M1/70, conjugated to PerCP/Cyanine5.5)	BioLegend	Cat#101228; RRID: AB_893232
Anti-CD71 (Clone RI7217, conjugated to FITC)	BioLegend	Cat#113806; RRID: AB_313567
Anti-Sca-1 (Clone D7, conjugated to FITC)	BioLegend	Cat#108106; RRID: AB_313343
Anti-c-Kit (Clone 2B8, conjugated to FITC)	BD Pharmingen	Cat#553354; RRID: AB_394805
Anti-CD45.2 (Clone 104, conjugated to FITC)	BD Pharmingen	Cat#553772; RRID: AB_395041
Anti-CD135 (Clone A2F10.1, conjugated to PE)	BD Pharmingen	Cat#553842; RRID: AB_395079
Anti-Streptavidin (conjugated to BV605)	BioLegend	Cat#405229
Anti-CD150 (Clone TC15-12F12.2, conjugated to BV605)	BioLegend	Cat#115927; RRID: AB_11204248
Anti-CD34 (Clone RAM34, conjugated to eFluor450)	Invitrogen	Cat#48-0341-82; RRID: AB_2043837
Anti-CD16/32 (Clone 2.4G2, conjugated to APC-R700)	BD Pharmingen	Cat#565502; RRID: AB_2739269
Anti-biotin (Clone Bio3-18E7.2, conjugated to microbeads)	Miltenyi Biotec	Cat#130-090-858
Anti-FITC microbeads	Miltenyi Biotec	Cat#130-048-701; RRID: AB_244371
Anti-BRD9	Abcam	Cat#ab259839
Anti-Actin	Sigma-Aldrich	Cat#1978; RRID: AB_476692
Bacterial and virus strains		
E. coli DH5α Competent Cells	Takara	Cat#9057
Chemicals, peptides, and recombinant proteins		
Mouse IL-3 Recombinant Protein	PeproTech	Cat#213-13-100UG
Mouse IL-6 Recombinant Protein	PeproTech	Cat#216-16-100UG
Mouse SCF Recombinant Protein	PeproTech	Cat#250-03-100UG
ACK lysis buffer	homemade	N/K
I-BRD9	Selleck	Cat#S7835
Critical commercial assays		
Methocult M3434	STEMCELL Technologies	Cat#03434
StemSpan SFEM	STEMCELL Technologies	Cat#09600

(*Continued on next page*)

Continued

REAGENT or RESOURCE	SOURCE	IDENTIFIER
Lymphoprep	STEMCELL Technologies	Cat#07801
IMDM	Sigma-Aldrich	Cat#I3390-500ML
FBS	Biowest	Cat#S1600-500
MACS LS columns	Miltenyi Biotec	Cat#130-042-401
RNeasy mini kit	Qiagen	Cat#74104
ATAC-seq kit	Active Motif	Cat#53150
Qubit dsDNA HS Assay Kit	Invitrogen	Cat#Q32851
RetroNectin Recombinant Human Fibronectin Fragment	Takara	Cat#T100B
Verso cDNA Synthesis Kit	Thermo Scientific	Cat#AB1453B
Deposited data		
Bulk RNA-seq	This study	GEO: GSE269210
Bulk ATAC-seq	This study	GEO: GSE269210
Single cell RNA-seq	This study	GEO: GSE269210
Experimental models: Organisms/strains		
C57BL/6J	Japan SLC, Inc.	N/A
Vav1-iCre; *Brd9*$^{fl/fl}$ mouse	This study	N/A
C57BL/6J (CD45.1)	Japan SLC, Inc.	N/A
Oligonucleotides		
Brd9 genotyping primer: PNDEL1 (5′-TGTGCCTAACAGGCTCACAA)	Xiao et al.[22]	N/A
Brd9 genotyping primer: PNDEL2 (5′-AGCAGGACTTTACCTCTCCCT)	Xiao et al.[22]	N/A
Brd9 recombination PCR primer: LOX1 (5′- AGTGACCTCAAGATTGCATGTTGG)	Xiao et al.[22]	N/A
Brd9 recombination PCR primer: PNDEL2 (5′- AGCAGGACTTTACCTCTCCCT)	Xiao et al.[22]	N/A
RT-PCR primer: Brd9 exon5 Fw (5′-ATCCTATGGACTTTGGCACG)	Xiao et al.[22]	N/A
RT-PCR primer: Brd9 exon6 Rv (5′-CTGGTCTATTGTACGTCATCGC)	Xiao et al.[22]	N/A
Vav1-iCre genotyping primer Fw (5′-CAGGTTTTGGT GCACAGTCA)	This study	N/A
Vav1-iCre genotyping primer Rv (5′-GGTGTTGTAGT TGTCCCCACT)	This study	N/A
RT-PCR primer: Gltscr1 Fw (5′-TGACACCTATTCAAGTGGTGGG)	This study	N/A
RT-PCR primer: Gltscr1 Rv (5′-CACCGAGTTCCCGTTGAGTG)	This study	N/A
shBrd9#1 (5′-TTTATT ATCATTGAATACCCAG)	Xiao et al.[22]	N/A
shBrd9#2 (5′-TTTATTTCTTCTTTCATCTTTG)	Xiao et al.[22]	N/A
shGltscr1#1 (5′-CGGTGGAGGATGAACTATATC)	Vector Builder	N/A
shGltscr1#2 (5′-GACAATTCTTGCCTAAGTTAT)	Vector Builder	N/A
Recombinant DNA		
pMIGII-BRD9 WT	Inoue et al.[23]	N/A
pMIGII-BRD9 dBD	Inoue et al.[23]	N/A
Software and algorithms		
ELDA: Extreme Limiting Dilution Analysis	Hu et al.[33]	https://bioinf.wehi.edu.au/software/elda/index.html
HISAT2 v2.2.1	Kim et al.[57]	https://daehwankimlab.github.io/hisat2/
featureCounts v2.0.6	Liao et al.[58]	https://bioconductor.org/packages/release/bioc/html/Rsubread.html

(*Continued on next page*)

Continued

REAGENT or RESOURCE	SOURCE	IDENTIFIER
edgeR v4.0.16	McCarthy et al.[59]	https://bioconductor.org/packages/release/bioc/html/edgeR.html
DESeq2 v1.46.0	Love et al.[60]	https://bioconductor.org/packages/release/bioc/html/DESeq2.html
Enrichr	Chen et al.[61–63]	https://maayanlab.cloud/Enrichr/
GSEA v4.2.3	Mootha et al.[64,65]	https://www.gsea-msigdb.org/gsea/index.jsp
Trimmomatic v0.39	Bolger et al.[66]	https://github.com/usadellab/Trimmomatic
Bowtie2 v2.4.4	Langmead et al.[67]	https://bowtie-bio.sourceforge.net/bowtie2/index.shtml
Picard v2.26.2	Broad Institute	https://broadinstitute.github.io/picard/
deepTools v3.5.1	Ramírez et al.[68]	https://deeptools.readthedocs.io/en/develop/index.html
MACS2 v2.2.7.1	Zhang et al.[69]	https://pypi.org/project/MACS2/
HOMER v4.11	Heinz et al.[41]	http://homer.ucsd.edu/homer/index.html
GREAT analysis	McLean et al.[50]	http://great.stanford.edu/public/html/index.php
IGV v2.16.2	Robinson et al.[70]	https://igv.org/doc/desktop/
Cell Ranger v7.1.0 and v7.2.0	10x Genomics	https://www.10xgenomics.com/jp/support/software/cell-ranger/downloads
Seurat v5.0.1	Hao et al.[71]	https://satijalab.org/seurat/
R v4.0.3, v4.2.3 and v4.3.3	R Core Team	https://www.R-project.org
Loupe Browser v7.0.1	10x Genomics	https://www.10xgenomics.com/jp/support/software/loupe-browser/downloads
CellRadar	Bagger et al.[44]	https://karlssong.github.io/cellradar/
cellDancer v1.1.7	Li et al.[48]	https://guangyuwanglab2021.github.io/cellDancer_website/
velocyto v0.17.17	La Manno et al.[72]	https://velocyto.org/velocyto.py/
scVelo v0.2.5	Bergen et al.[73]	https://scvelo.readthedocs.io/en/stable/index.html
ARTool v0.11.1	Kay et al.[74]	https://depts.washington.edu/acelab/proj/art/
Biorender	BioRender	https://BioRender.com
GraphPad Prism v10	Graphpad Software	https://www.graphpad.com

EXPERIMENTAL MODEL AND STUDY PARTICIPANT DETAILS

Animals

All animal procedures were performed in accordance with the Guidelines for the Care and Use of Laboratory Animals and approved by the Institutional Animal Care and Use Committees of the Foundation for Biomedical Research and Innovation (FBRI, Japan). Also, all mouse experiments were performed in strict accordance with protocols approved by the FBRI Institutional Animal Care and Use Committee (Study approval numbers: 22-10 and 24-08). All animals were housed at FBRI using a 12-h light/12-h dark cycle at an ambient temperature of 72°F ± 2°F (~21.5°C ± 1°C) with 30–70% humidity. All mice used in this study are in C57BL/6J Jms background. To obtain fetal livers (FL), mating pairs were setup between 10-week-old *Brd9*$^{fl/fl}$ male mice and 10-week-old *Vav1*-iCre; *Brd9*$^{fl/fl}$ female mice. Mouse pregnancy was checked by vaginal plug and the day confirmed was counted as E0.5. Fetal livers were obtained on E14.5. In the analysis of experiments, male and female fetuses were not differentiated. In transplantation assay, both 10-week-old male and female CD45.1^{+} recipient mice were used for analysis. Detailed mouse numbers used for each analysis are reported in the related figure legends. For transplant recipients, we employed both male and female mice across a distinct series of transplant experiments. The analysis revealed no significant differences in outcomes based on the sex of the mice. Consequently, we integrated the data from both groups in the results section.

Generation of *Vav1*-iCre; *Brd9*$^{fl/fl}$ mice

Brd9 floxed allele contains the *LoxP* cassette and the targeted region is ~2.4 kb including exons 4–6 corresponding its bromodomain.[21] *Brd9* floxed mice were genotyped by PCR with primers PNDEL1 (TGTGCCTAACAGGCTCACAA) and PNDEL2 (AGCAGGACTTTACC TCTCCCT) using the following parameters: 94°C for 2 min, flowed by 30 cycles of 94°C for 45 s, 60°C for 30 s, and 72°C for 1 min, and then 72°C for 7 min. The *Brd9* floxed and WT alleles were detected as 505 bp and 626 bp bands,

respectively. *Brd9*$^{fl/fl}$ mice were mated with *Vav1*-iCre mice for several generations to obtain *Vav1*-iCre; *Brd9*$^{fl/fl}$ mice. Successful recombination of *Brd9* was validated by PCR with primers LOX1 (AGTGACCTCAAGATTGCATGTTGG) and PNDEL2 (AGCAGGACTTTACCTCTCCCT). Total RNA was isolated using RNeasy Mini kit (Qiagen). For cDNA synthesis, total RNA was reverse transcribed to cDNA with Verso cDNA Synthesis Kit. *Brd9* expression was investigated by qRT-PCR with primers *Brd9* exon5 Fw (ATCCTATGGACTTTGGCACG) and *Brd9* exon6 Rv (CTGGTCTATTGTACGTCATCGC).

METHOD DETAILS

Isolation of mouse fetal liver, bone marrow and spleen cells

On E14.5, the pregnant mouse was sacrificed, and fetuses were separated from the uterus and placed in ice-cold phosphate-buffered saline (PBS) with 1% fetal bovine serum (FBS). A single cell suspension from the fetal liver was mechanically homogenized with a 23-gauge needle. Mononuclear cells were harvested by performing density gradient centrifugation (Lymphoprep, STEMCELL Technologies) and then proceeded to sequent experiments. Bone marrow (BM) and spleen cells were harvested from adult mice aged more than 20 weeks. Freshly dissected femora and tibiae were isolated, and BM was flushed with a 3 mL insulin syringe into PBS supplemented with 1% FBS. The BM was spun at 500g by centrifugation and Red blood cells (RBCs) were lysed in ammonium chloride-potassium bicarbonate (ACK) lysis buffer for 5 min. After centrifugation, cells were resuspended in PBS plus 1% FBS, passed through a cell strainer, and counted. Spleen was dissected from a mouse and smashed through a 40 μm cell strainer to harvest single cells. RBCs were lysed in ACK lysis buffer for 5 min. After centrifugation, cells were resuspended in PBS plus 1% FBS, passed through a cell strainer, and counted.

Flow cytometry, FACS sorting and Western blot analysis

Fluoroprobe conjugated and biotinylated antibodies used in this study are listed in key resources table. The cells were stained in PBS with 1% FBS unless otherwise stated. Through the whole procedure, the staining buffer was kept ice-cold, and the cells were stained for 30 min at 4°C in the dark. In case when the primary biotinylated antibodies were used, a secondary staining was performed with streptavidin-BV605 or PerCP-Cy5.5. Following biotin-conjugated antibodies were used to label lineage positive cells: anti-CD3ε, anti-CD4, anti-CD8a, anti-CD19, anti-NK1.1, anti-Gr-1, anti-Ter-119. HSPCs were stained with antibodies against Sca-1, c-Kit, CD135, CD150, CD48, CD34, CD16/32, CD127. For evaluating erythroid maturation, cells were firstly labeled with biotin-conjugated antibodies against B220, Gr-1, CD3ε and fluorescence-conjugated antibodies against CD71 and Ter-119. Then cells were secondarily stained with streptavidin-PerCP-Cy5.5. For splenocytes FACS analysis, splenocytes were labeled with antibodies against CD45.2, Gr-1, CD11b, B220, CD3ε. Antibodies against BRD9 (abcam; ab259839; 1:1000) and Actin (Sigma-Aldrich, A1978, 1:5000) were used in Western blot analysis.

Colony formation assay

Lineage negative (Lin$^-$) population was selected by MACS depletion. In detail, single cells were suspended in PBS with 1% FBS containing the following primary biotin-conjugated antibodies: anti-CD3ε, anti-CD4, anti-CD8a, anti-CD19, anti-NK1.1, anti-Gr-1, anti-Ter-119. Anti-biotin microbeads (Miltenyi Biotec, #130-090-858) were used as secondary antibodies. Negative selection was performed to enrich Lin$^-$ cells. Lin$^-$ cells were resuspended in IMDM/2% FBS medium and cell number was counted. Lin$^-$ cells were seeded at a density of 1000 cells/replicate into cytokine-supplemented methylcellulose medium (Methocult M3434, STEMCELL Technologies). Colonies propagated in culture were scored at day 7–10.

I-BRD9 treatment

E14.5 FL cells were isolated from wild-type C57BL/6J pregnant mouse. Lin$^-$ cells were obtained through the Lineage Cell Depletion kit (Miltenyi Biotec). Lin$^-$ cells were cultured at a density of 1 × 10^5/mL in StemSpan SFEM media containing 10 ng/mL mouse interleukin (IL)-3, 10 ng/mL mouse IL-6, and 20 ng/mL mouse stem cell factor (SCF). Cells were divided into four groups and treated with different concentrations of I-BRD9 (DMSO as control, 100 nM, 1 μM, and 10 μM). After 5 days of treatment, cells were reseeded at equal numbers into cytokine-supplemented methylcellulose medium (Methocult M3434, STEMCELL Technologies) with the respective concentrations of I-BRD9. Colonies were scored after 7–10 days of culture.

Retroviral transduction

E14.5 FL cells were isolated from wild-type C57BL/6J pregnant mouse (for shRNA knock-down) or *Brd9*$^{fl/fl}$ (Control) pregnant mouse, as well as *Vav1*-iCre; *Brd9*$^{fl/fl}$ (*Brd9* KO) pregnant mouse (for BRD9 addback). Lin$^-$ cells were obtained through the Lineage Cell Depletion kit (Miltenyi Biotec). The cells were then subjected to retroviral transduction using Retronectin. Cells derived from wild-type C57BL/6J mice were transduced with viral supernatants containing sh*Brd9* or sh*Gltscr1*, while cells from Control and *Brd9* KO were transduced with viral supernatants containing empty vector, full-length *BRD9* cDNA (BRD9 WT), or bromodomain-dead mutant *BRD9* cDNA (dBD). All vectors were labeled with GFP. Cells were incubated in StemSpan SFEM media supplemented with 10 ng/mL mouse IL-3, 10 ng/mL mouse IL-6, and 20 ng/mL mouse SCF. Within 48 h, GFP-positive cells were FACS-sorted and reseeded in equal numbers into cytokine-supplemented methylcellulose medium (Methocult M3434, STEMCELL Technologies). Colonies were scored after 7–10 days of culture.

Transplantation assay and limiting dilution assay

E14.5 Lin$^-$ FL cells and LK/LSK FL cells were harvested as above described and transplanted via tail vein injection into lethally irradiated (4.5 Gy × 2) CD45.1$^+$ recipient mice. LK cells were transplanted at 70K cells per recipient mouse, and LSK cells at 3K cells per mouse. To perform the limiting dilution assay, recipients were transplanted with different cell numbers, which were 50K cells/mouse, 200K cells/mouse and 400K cells/mouse, respectively. The analysis of the limiting dilution assay was performed on https://bioinf.wehi.edu.au/software/elda/index.html.

Bulk RNA-seq

For sorted E14.5 FL cells (live Lin$^-$ cells), RNA was extracted using RNeasy columns (Qiagen) according to manufacturer's instructions. RNA was then Poly(A)- selected, and stranded Illumina libraries were prepared using TruSeq Stranded mRNA Library Prep Kit. The libraries were sequenced with illumina NovaSeq 6000 at a depth of ~30 M 2 × 151 bp reads per sample. For differential expression analysis, sequenced reads were mapped to mm10 using HISAT2.[57] Gene counts were calculated with featureCounts[58] and differentially expressed genes were identified with Adjusted p value <0.05 by edgeR 4.0.16.[59] Variance stabilizing transformed gene counts was used for principal component analysis.[60] With differentially expressed gene sets, gene ontology (GO) and gene set enrichment analysis (GSEA) pathway analysis was performed by Enrichr[61–63] and GSEA software.[64,65]

ATAC-seq

ATAC-seq library preparation was performed on FACS-sorted Lin$^-$c-Kit$^+$ E14.5 FL HSPCs (150,000 cells per sample) using the ATAC-seq kit from Active motif (#13150). The QC of DNA libraries was analyzed on an Agilent Technologies 2100-Bioanalyzer, using a High Sensitivity DNA chip. The libraries were quantified using the Qubit dsDNA HS Assay Kit (Thermo Fisher Scientific). The ATAC-Library was sequenced with a NovaSeq 6000 platform (Illumina) at a depth of ~39 M 2 × 150 bp read pairs per sample. Reads were quality filtered according to the standard Illumina pipeline, de-multiplexed and FASTQ files were generated. The adapter sequences were removed from the ATAC-seq FASTQs using Trimmomatic (0.39)[66] with the options ILLUMINACLIP: NexteraPE-PE.fa:2:30:10 LEADING:30 TRAILING:30 SLIDINGWINDOW:4:15 MINLEN:50 on the PE mode. The cleaned FASTQs were aligned using Bowtie2 (2.4.4)[67] to the mouse reference genome mm10 with the parameters -X 2000 –no-discordant –no-mixed –dovetail –very-sensitive and the duplicated reads were removed using picard (2.26.2) MarkDuplicates with REMOVE_DUPLICATES = true. BigWig files were generated from the bam files using bamCoverage[68] with the parameters –ignoreDuplicates –normalizeUsing RPGC –effectiveGenomeSize 2000000000 –binSize 1 –ignoreForNormalization chrX. Peaks were called using macs2 (2.2.7.1)[69] callpeak with -f BAMPE -g mm –nomodel –keep-dup-all parameters. Then, peaks were merged using mergePeaks[41] -d given and a venn diagram was drawn. Motifs for Control and KO specific peaks were searched with findMotifsGenome.pl program[41] with mm10 -size given parameters. For analysing duplicated samples, consensus peaks were identified using mergePeaks -d given and signal intensities of consensus peaks were calculated by geometric mean. With signal intensities calculated using multiBigwigSummary[68] BED-file, differential peaks were determined with a fold-change threshold 1.5 and analyzed with GREAT.[50] For comparing ATAC peaks of FL and bone marrow (BM) HSPCs, bigWig files were generated from FASTQs used in our previous work (GSE203315)[22] and visualized with IGV.[70] To identify super-enhancer (SE) and typical enhancer (TE), H3K27Ac and Input ChIP-seq FASTQs derived from FL HSC were obtained from GSE119200, and processed in the similar way[22] except that we adjusted the parameters on SE mode, for expample, ILLUMINACLIP:TruSeq3-SE.fa:2:30:10 LEADING:30 TRAILING:30 SLIDINGWINDOW:4:15 MINLEN:30 on the SE mode were used as trimmomatic parameters.

Single cell RNA-seq library preparation

Single cell RNA-seq libraries of FACS-sorted Lin$^-$c-Kit$^+$ E14.5 FL HSPCs were prepared according to the manufacturer's protocol using the 10x Genomics Chromium Next GEM Single cell 3′ Kit v3.1 and Dual Index Kit. The libraries were sequenced with NovaSeq 6000 (Illumina) at a depth of 450M reads per sample. Raw sequencing data were demultiplexed and converted to the standard FASTQ files by executing cellranger mkfastq (7.1.0, 10x Genomics). For analyzing Lin$^-$Kit$^+$ BM HSPCs, FASTQs (GSE203321)[22] were also analyzed. Gene counts of each sample were generated by cellranger count (7.2.0, 10x Genomics) with mm10-2020A as the reference dataset. For each sample, over 7000 cells were retrieved, where 50000 mean reads and 5000 median genes were obtained per cell. The filtered feature barcode matrices were analyzed using Seurat (5.0.1) R package[71] on R (4.2.3) (https://www.R-project.org; 2022). After calculating QC metrics, low quality cells not meeting the following criteria were removed: 3000 $\leq$ nCount_RNA <120000 (FL) or 8000 (BM), 1000 $\leq$ nFeature_RNA <9000 (FL) or 8250 (BM), and 0 $\leq$ percent.mt < 7. As a result 29591 cells were retained. NormalizeData function with normalization.method = ''LogNormalize'' and scale.factor = 10000 was performed. Then, FindVariableFeatures with selection.method = ''vst'' nfeatures = 3000 and ScaleData function with vars.to.regress = ''percent.mt'' was applied for the fist scaling. Cell cycle scores were calculated by CellCycleScoring function with cc.genes.updated.2019 cell cycle genes, where differences of cell cycle scores (CC.Difference) between S phase and G2M phase were obtained, and ScaleData function with vars.to.regress = c (''percent.mt'', ''CC.Difference'') was applied for the second scaling. Finally, each data were integrated through executing IntegrateLayers function with method = ''CCAIntegration'' normalization.method = ''LogNormalize'' dims = 1 : 100. Principal component analysis (PCA) was performed with the integrated data followed by FindNeighbors, FindClusters and uniform manifold approximation and projection (UMAP) dimensional reduction. Cell clusters and UMAP coordinates were exported from the Seurat object and imported into the Loupe Browser file created by cellranger aggr for

following analyses and visualization. Cell types were manually assigned to each cluster, and percentages of cell types were calculated. Differentially expressed genes compared *Brd9* KO to Control on each cell type were determined using FindMarkers with non-parametric Wilcoxon rank-sum test and p value <0.01. Gene ontology (GO) analysis was performed by Enrichr.[61–63] Normalized expressions of cell type specific genes were visualized by DotPlot function.

CellRadar (using data from HemaExplorer,[44] https://karlssong.github.io/cellradar/) was used to investigate lineage affiliation and to create a radar plot using marker genes (adj p value <0.05 calculated with Loupe Browser) in related clusters.

RNA Velocities were estimated using cellDancer (1.1.7) following to the instruction.[48] Briefly, loom file was generated from the bam file of each sample using velocyto (0.17.17)[72] run and adata file of each sample was exported from the integrated Seurat object. The loom files and adata files were processed with scVelo (0.2.5)[73] by applying scv.pp.filter_and_normalize and scv.pp.moments functions. The processed data were further analyzed with cellDancer by applying cdutil.adata_to_df_with_embed, cd.velocity and cd.compute_cell_velocity functions. The estimated cell velocities were visualized using cdplt.scatter_cell function.

QUANTIFICATION AND STATISTICAL ANALYSIS

Statistical analyses were performed using HOMER (version 4.11), MACS2 (version 2.2.7.1), cellranger (version 7.2.0), R (version 4.0.3, 4.2.3, and 4.3.3), ARTool (version 0.11.1, https://github.com/mjskay/ARTool),[74] GraphPad Prism (version 10), edgeR (version 4.0.16) and GSEA (version 4.2.3) software. Statistical significance was calculated using two-tailed unpaired t-test, log rank test, negative binomial test (adjusted using the Benjamini-Hochberg correction), two-sided Wilcoxon rank-sum test, Tow-way ANOVA with Aligned Rank Transform, GSEA, binomial distribution in HOMER, ELDA, GREAT, Enrichr, and indicated in the figure legend. Statistical significance was set as *: $p < 0.05$, **: $p < 0.01$, ***: $p < 0.001$, ****: $p < 0.0001$; ns: not significant ($p > 0.05$). The number of mice in each group and the number of replicates for each experiment are indicated in the legends of the main and supplemental figures. All error bars represent mean ± s.e.m.